ISPRS Journal of Photogrammetry and Remote Sensing 191 (2022) 49–67

Contents lists available at ScienceDirect

ISPRS Journal of Photogrammetry and Remote Sensing

journal homepage: www.elsevier.com/locate/isprsjprs

An improved approach of dry snow density estimation using C-band synthetic aperture radar data

Min Li [a,b], Pengfeng Xiao [a,c,*], Xueliang Zhang [a], Xuezhi Feng [a], Liujun Zhu [d]

[a] Jiangsu Provincial Key Laboratory of Geographic Information Science and Technology, Key Laboratory for Land Satellite Remote Sensing Applications of Ministry of Natural Resources, School of Geography and Ocean Science, Nanjing University, Nanjing, Jiangsu 210023, China
[b] School of Urban Construction, Heze University, Heze, Shandong 274015, China
[c] Jiangsu Center for Collaborative Innovation in Geographical Information Resource Development and Application, Nanjing, Jiangsu 210023, China
[d] Yangtze Institute for Conservation and Development, Hohai University, Nanjing, Jiangsu 210023, China

A R T I C L E I N F O

Keywords:
Dry snow density
Relative permittivity
C-band SAR
Scattering simulation

A B S T R A C T

Snow density is one of the important indicators of snow cover hydrological potential. The application of existing algorithms for retrieving dry snow density using synthetic aperture radar (SAR) data is limited by single scattering mechanism, small terrain fluctuation or narrow incidence angle range. In the study, an improved approach was proposed to retrieve dry snow density from C-band SAR data with a wide range of roughness and local incidence angles. Both the snow-ground interface scattering and volume scattering were considered in the approach. First, the relationship between the backscattering at the snow-ground interface and relative permittivity was obtained based on simulation using the Advanced Integral Equation Model (AIEM) and regression analysis. Then the classical relationship between the volume backscattering and relative permittivity obtained by the first-order volume scattering model was incorporated into the approach. For comparison, the coefficients of the Shi algorithm were redefined by the AIEM model and regression analysis, and the Shi algorithm initially developed for L-band was modified for C-band. In experiments, the RADARSAT-2 data obtained in the Manasi River Basin on December 12–17, 2013 and the C-band GaoFen-3 data obtained in the Kelan River Basin on January 17, 2018 were selected to validate the applicability of the proposed approach under different conditions. The inversion results in the Manasi River Basin using the proposed approach, Singh algorithm, and modified Shi algorithm were compared. The results in the Manasi River Basin show that the correlation coefficients (Rs) between the measured and estimated dry snow density are 0.868, 0.694, and 0.653 for the three methods, respectively. The root mean square errors (RMSEs) are 31.1 kg m^{-3}, 59.1 kg m^{-3}, and 64.7 kg m^{-3}, respectively, and the mean relative errors (MREs) are 12.9%, 21.9%, and 25.5%, respectively. The corresponding R, RMSE, and MRE in the Kelan River Basin using the proposed approach are 0.717, 57.2 kg m^{-3}, and 27.1%, respectively. The results prove that the dry snow density under different C-band SAR data and different areas can be effectively retrieved using the proposed approach superior to the other two algorithms.

1. Introduction

Seasonal snow cover is one of the most active natural elements, which not only affects changes in the environment and the climate (Brucker et al., 2011; Zhong et al., 2014), but also serves as the main supply of fresh water resources in arid and semi-arid areas. Snow water equivalent (SWE) is an important parameter for evaluating the contribution of seasonal snow cover to water resources or evaluating the hydrological potential of snow cover (Varade et al., 2020a). SWE indicates the amount of liquid water stored in snow (Singh et al., 2017). It is the product of snow density and depth. Since the microwave spectrum of remote sensing may not fully penetrate the wet snow cover, this study was focused on the dry snow. Fortunately, the density of dry snow can be sufficient for the estimation of SWE because the SWE change little when the snow transits from dry to wet if the water balance of the snow cover is kept. In the past, dry snow density was rarely taken seriously and generally assumed to be a constant value when estimating SWE on a large scale (Jonas et al., 2009; Singh et al., 2017). However, dry snow

* Corresponding author at: Jiangsu Provincial Key Laboratory of Geographic Information Science and Technology, Key Laboratory for Land Satellite Remote Sensing Applications of Ministry of Natural Resources, School of Geography and Ocean Science, Nanjing University, Nanjing, Jiangsu 210023, China.
E-mail address: xiaopf@nju.edu.cn (P. Xiao).

https://doi.org/10.1016/j.isprsjprs.2022.07.002
Received 24 August 2021; Received in revised form 1 February 2022; Accepted 6 July 2022

density varies greatly with time and space in mountain areas, thus snow depth information alone is insufficient to determine SWE (Gray, 1970; Singh et al., 2017). In addition, the retrieval of snow depth is significantly affected by dry snow density (Guneriussen et al., 2001; Li et al., 2017; Varade et al., 2020a). Snow density is a fundamental physical property of snow cover. In addition to playing a crucial role in calculating SWE (Bernier and Fortin, 1998; Elder et al., 1991; Sturm et al., 2010), it is also useful for simulating snowmelt runoff (DeBeer and Pomeroy, 2010; Martinec and Rango, 1986), estimating snow load (Meloysund et al., 2007), and predicting avalanches (Brun et al., 1992; Hirashima et al., 2009). Unfortunately, sparse weather stations make it impractical to collect enough field measurements. Therefore, alternative methods from remote sensing data provide a more feasible way to exploit snow density in environmental and hydrological studies.

Active microwave remote sensing, especially synthetic aperture radar (SAR), has been an effective way to obtain snow parameters due to its good penetration ability, sensitivity to the dielectric and geometric properties of snow, and high spatial resolution (Shi et al., 2012). Some recent studies applied full-polarized backscattering coefficients or phase information in snow properties estimation, with encouraging results. Ma et al. (2020) retrieved snow wetness in Xinjiang, China using fully polarized SAR data. Santi et al. (2021) evaluated the ability of ANN to retrieve snow depth and snow water equivalent from X-band and Ku-band SAR data. Conde et al. (2019) used spaceborne SAR interferometry to estimate the temporal variation of snow water equivalent. And Varade et al. (2020b) estimated the snow depth in Dhundi based on weighted bias corrected differential phase observations of dual-polarization bi-temporal Sentinel-1 data. Despite the great advance, these methods commonly involved complex processes and required well calibrated SAR data in both amplitude and phase, with few applications in the estimation of snow density. A simple and straightforward method based on snow scattering models is still a promising alternative in this stage.

The penetration depth of microwaves to dry snow is inversely proportional to the wavelength (Shi and Dozier, 2000), and the backscattering of dry snow is mainly attributed to dry snow density (Abe et al., 1990; Shi and Dozier, 2000; Singh et al., 2017). The received total backscattering of snow cover can be decomposed into air-snow interface backscattering, the snow volume backscattering, and the snow-ground interface backscattering (Ulaby et al., 1982). Owing to the small dielectric contrast at the air-snow interface, the contribution of air-snow interface may be overlooked for the angles away from nadir (Ulaby et al., 1982). Regarding dry snow, the snow-ground interface backscattering is particularly important due to the strong penetration of microwave into the dry snow layer (Ma et al., 2020). The volume backscattering should also be considered because of the potential variation of inner snow permittivity.

Several algorithms have been developed to reckon snow density from SAR data. The principle in common is to firstly separate the surface and volume scattering. Secondly, various methods are used to find out the suitable relationship between surface or volume scattering and snow relative permittivity (Shi and Dozier, 1995; Shi et al., 1990). Then snow density is retrieved. Therefore, the establishment of accurate relations is vital to the inversion of snow density.

Most algorithms only considered a single scattering mechanism of surface or volume backscattering. Shi and Dozier (2000) used the integrated equation model (IEM) (Fung, 1994; Fung et al., 1992) and regression analysis to build a simplified relationship between the snow-ground interface backscattering under the conditions of changes in various parameters and relative permittivity, which was used to invert dry snow density from SIR-C L-band data. The algorithm was successfully applied in the American Mammoth Mountain (Shi and Dozier, 2000) and the Chinese Tianshan Mountains (Li et al., 2001) where the underlying surface is soil or rock. Awasthi et al. (2020) estimated the snow density in the North-Western Himalayas obtaining the relationship between surface backscattering and relative permittivity using the IEM model (Fung, 1994; Fung et al., 1992) with C-band RISAT-1 datasets. Surendar et al. (2015) contacted volume backscattering and relative permittivity using the generalized four component polarimetric decomposition with unitary transformation (G4U) (Singh et al., 2013) to reverse dry snow density with C-band RADARSAT-2 data in the Indian Himalayas where the snow cover is over sparse vegetation. Singh et al. (2017) contacted volume backscattering and relative permittivity using the generalized Singh-Cloude three-component hybrid decomposition method (GS3H) (Singh et al., 2017) for the retrieval of dry snow density based on TerraSAR-X data in the Himalayas. Varade et al. (2020a) used bi-temporal C-band RADARSAT-2 data to estimate the early winter snow density in the Himalayas considering the relationship between volume backscattering and relative permittivity. Nevertheless, snow density inversion will be affected only considering surface or volume backscattering.

One step further, the modified algorithm considered the associations between surface and volume scattering and snow relative permittivity to infer snow density. Singh and Venkataraman (2009) gained the affiliations between volume backscattering and snow-ground interface backscattering and relative permittivity apart on the basis of the first-order scattering model and the small perturbation model (SPM) (Valenzuela, 1967) to build an inversion model, in turn derived dry snow density by C-band ENVISAT-ASAR data. The algorithm was applicable to the Indian Himalayan region where the underlying surface is bare soil or rock (Singh and Venkataraman, 2009; Venkataraman et al., 2010). However, the SPM (Valenzuela, 1967) is available for slightly rough surfaces (Engman and Chauhan, 1995), and the algorithm was fit to a narrow range of incidence angles, limited to 31.0°–36.3°.

Naturally, dry snow density can be better retrieved under the overall consideration of scattering mechanism. The backscattering of dry snow is sensitive to surface roughness. The underlying surface is continuously distributed, including various levels of roughness. Moreover, the complex terrain in the mountains will result in a wide range of incidence angles. The above-mentioned algorithms only think about part of the influencing factors on dry snow density inversion. How to fully consider the scattering mechanism and the large-scale surface roughness and incidence angles on the complex mountain terrain at the same time is still unsolved.

In the study, we propose an improved approach for retrieving dry snow density using C-band SAR data. Both the snow-ground interface backscattering and volume backscattering are considered in the approach. Moreover, the range of surface roughness and incidence angle under conditions of complex terrain in the mountains is fully considered for an enhanced method with a much wider range of validity. The core of this study is to find a new and more suitable affiliation between surface backscattering and relative permittivity with the Advanced Integral Equation Model (AIEM) (Chen et al., 2000; 2003). AIEM can reproduce the real surface scattering in a broad scope of surface roughness. It has become a universal model dealing with electromagnetic scattering from terrain surfaces in recent years. In addition, the dry snow density inversion algorithm for L-band data developed by Shi and Dozier is modified for C-band data using AIEM. Finally, the proposed approach is compared with the Singh algorithm (the dry snow density estimation algorithm developed by Singh and Venkataraman) (Singh and Venkataraman, 2009) and the modified Shi algorithm (the modified dry snow density estimation algorithm developed by Shi and Dozier (2000)) to demonstrate its superiority. Furthermore, two types of study areas and SAR data are selected to validate the applicability of the proposed approach.

2. Study areas and data

2.1. Study areas

Xinjiang Province is one of the three major snow-covered areas in China (Ma et al., 2020). There are Kunlun, Tianshan, and Altay

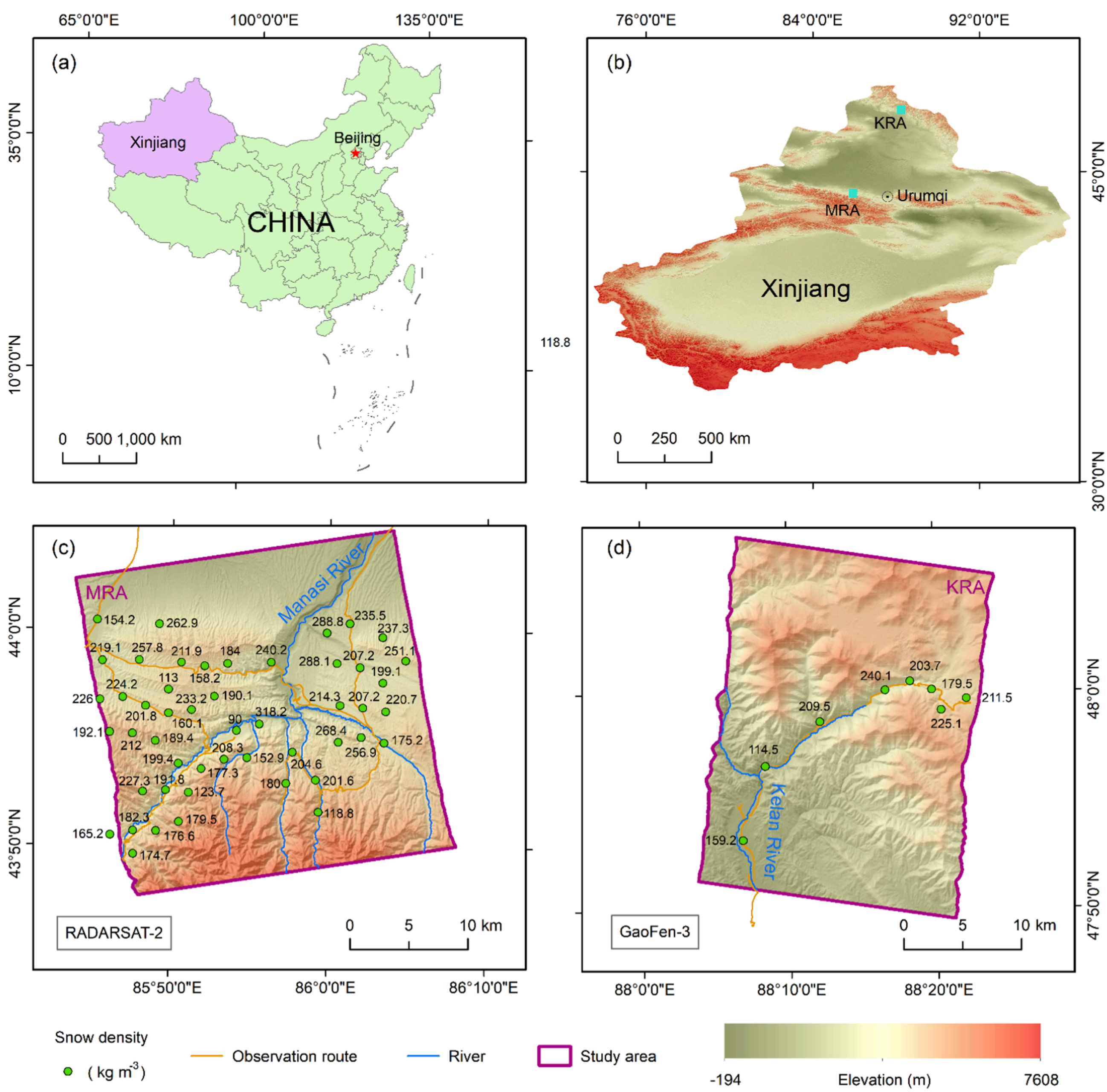

Fig. 1. Location of the two study areas MRA and KRA in the Manasi River Basin and Kelan River Basin, Xinjiang Province, China, respectively (a, b), and the snow density of sample points of field measurements (c, d).

Table 1
Parameters of the two SAR data.

Satellite	Centre frequency (GHz)	Acquisition time (UTC + 8)	Beam mode	Pixel spacing (m)		Centre incidence angle (°)
				Slant range	Azimuth	
RADARSAT-2	5.405 (C-band)	2013.12.13 20:16	Fine quad-pol	4.733	4.779	43.45
GaoFen-3	5.4 (C-band)	2018.01.17 00:12	QPSI	2.248	4.869	43.96

Mountains from south to north in Xinjiang Province. The terrain, climate, and snow characteristics vary with different mountains. Consequently, we select two study areas in Manasi River Basin (MRA) of Tianshan Mountains and Kelan River Basin (KRA) of Altay Mountains (Fig. 1). The purpose is to verify the adaptability of the proposed approach under different conditions.

The MRA covered by RADARSAT-2 satellite data is situated in the Manasi River Basin originating from the northern piedmont of Tianshan Mountains, at 43°48′–44°05′ N, 85°44′–86°08′ E. The terrain is high in the south and low in the north. The elevation difference is about 2000 m and the average elevation is 2936 m. The annual average temperature is 6.5 °C (Ma et al., 2020). The snow cover has the characteristics of thin thickness and low density. It appears in November, peaks in February, and decreases in March (Dai et al., 2012; He et al., 2015).

The KRA covered by GaoFen-3 satellite data is located in the Kelan River Basin originating from the southern piedmont of Altay Mountains,

Table 2
Soil parameters used to simulate the backscattering components at snow-ground interface.

Soil parameters	Minimum	Maximum	Interval
Volumetric water content (%)	2	50	2
RMS height (cm)	0.2	4	0.2
Correlation length (cm)	2.5	35	10
Local incidence angle (°)	20	71	1
Wavenumber (cm^{-1})	1.211	1.420	0.009
Correlation function	Exponential		

at 47°49′–48°07′ N, 88°03′–88°24′ E. Contrary to MRA, the terrain is high in the north and low in the south. The elevation difference is about 2500 m with an average elevation of 1174 m. The annual average temperature is 5.2 °C (Ma et al., 2020), 1.3 °C lower than that in MRA. The snow cover appears in mid or late October and melts in late March or early April (Ma et al., 2020). The annual average snow depth exceeds 40 cm (Zhuo et al., 2017), being twice of that in MRA.

2.2. SAR data and data preprocessing

RADARSAT-2 and GaoFen-3 data were used in this study synthetically considering the spatial resolution of data, the temporal and spatial distribution of snow, and the feasibility of synchronous observation experiments. The specific parameters of the two SAR data are listed in Table 1.

In order to retrieve snow density, the single-look complex (SLC) data were first averaged to form multi-look images having larger azimuth and range pixel spacing. The azimuth and range pixel spacing were 9.559 m and 6.882 m obtained from the RADARSAT-2 data with a window of 2 × 1 pixels. The corresponding values were 9.738 m and 6.745 m obtained from the GaoFen-3 data with a window of 2 × 3 pixels. Then the Frost filter (Frost et al., 1982) with a window of 9 × 9 pixels was performed to reduce image speckles. The Range-Doppler terrain correction was further carried out with the SRTM V1 data to generate the local incidence angle maps and to mask out the layover/shadow areas.

2.3. Field measurement data

In consideration of the requirements of observation data, accessibility of vehicles, and actual workload, the observation routes were selected in MRA and KRA (Fig. 1). Vertical profiles of the snow cover (snow pits) were first made at the observation points (Fig. 2). Then the snow and soil features were measured including snow density, free liquid water content of snow, snow temperature, snow grain size, snow depth, soil root mean square (RMS) height, and soil correlation length. The first four features were layered observations. The stratified density was measured with a snow fork. It obtains the complex relative permittivity of snow and then calculates the snow density by a semi-empirical formula (Sihvola and Tiuri, 1986). It is widely used for in-situ measurements of snow (Techel et al., 2011b).

In MRA, field measurements were carried out during December 12–17, 2013. On December 12, there was a light snowfall in parts of the

Table 3
Parameters used to simulate the snow volume backscattering components.

Parameters	Minimum	Maximum	Interval
Volumetric water content of soil (%)	2	50	2
Local incidence angle (°)	20	71	1
Snow density (kg m^{-3})	90	320	10
Radar frequency (GHz)	5.405		
Snow depth (cm)	8.66		
Snow temperature (K)	268.96		
Snow grain diameter (mm)	0.8		
Volumetric water content of snow (%)	0		
QCA stickiness parameter	0.1		

(a) MRA (b) KRA

Fig. 2. Field photographs in MRA (a) and KRA (b).

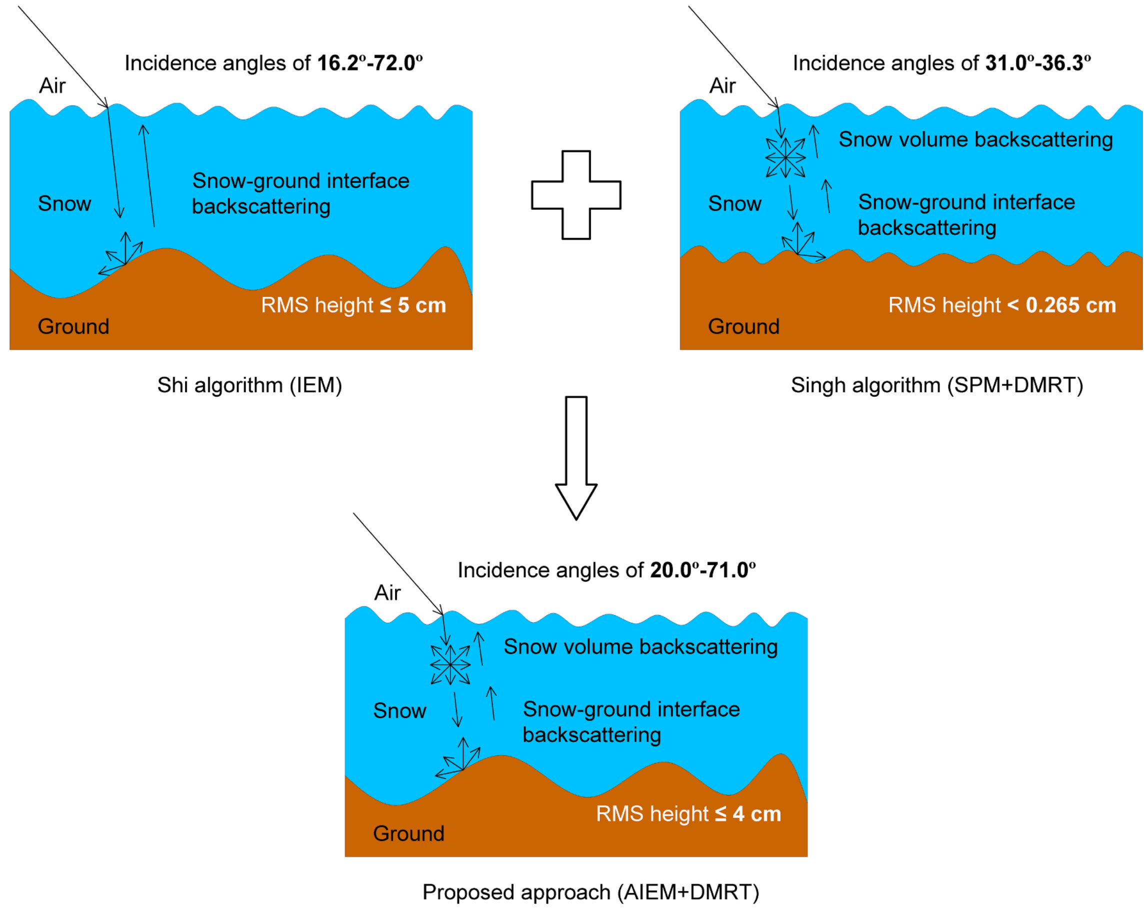

Fig. 3. Schematic diagram of the proposed dry snow density inversion approach.

area, that stopped just before the RADARSAT-2 transit. 13 snow pits were made and the interval of stratified observation was 5 cm. The results showed that the snow was shallow, mostly with 2 layers. It was mainly coarse-grained snow, with a grain diameter of 0.8 mm. The volumetric water content of the rest snow pits was 0 except that of two snow pits were 0.35% and 0.23%, respectively (Table A1). As a result, the snow in MRA was dry during imaging. So as to better understand the spatial distribution of snow cover, 36 other flat sites were chosen to measure the snow density and depth through snow tube, electronic scale, and ruler. Fig. 1 presents the snow density at 49 sampling points. It is shown that the distribution range of dry snow density in MRA was wide.

In KRA, field measurements were carried out on January 17, 2018 (the day of GaoFen-3 transit). 8 snow pits were made and the interval of layered observation was 10 cm. The results showed that the snow was deep, mostly with more than 6 layers. It was mainly coarse-grained snow, with a grain diameter of 0.9 mm. The minimum and maximum volumetric water content of the snow pits were 0.04% and 1.19%, respectively (Table A1). As a result, the snow in KRA was not entirely dry during imaging. A small amount of liquid water exists at the bottom of most sample points, which has little effect on the inversion results. However, there is a little more liquid water in the bottom or middle layer of individual points, which will have a certain impact on the inversion results. Fig. 1 shows the snow density at 8 sampling points.

3. Methodology

3.1. Proposed approach

The improvements in the proposed approach are illustrated in Fig. 3.

Assuming that the dry snowpack does not have obvious air-snow scattering and the volume extinction

is small at C-band, the total backscattering mainly contains two components (Fung, 1994; Shi et al., 1990):

$$\sigma_t^{pp}(\theta_i) = \sigma_v^{pp}(\theta_r) + T_{pp}^2(\theta_i)\sigma_{sg}^{pp}(\theta_r), \tag{1}$$

where $\sigma_t^{pp}(\theta_i)$ is the total backscattering coefficient for polarization pp with θ_i denoting the local incidence angle at the air-snow interface. $\sigma_v^{pp}(\theta_r)$ and $\sigma_{sg}^{pp}(\theta_r)$ are the volume and snow-ground interface backscattering coefficient for polarization pp with θ_r denoting the refractive angle at the air-snow interface, respectively. T_{pp} is the Fresnel power transmissivity at the air-snow interface for polarization pp.

The square root of the product of VV and HH polarization backscattering coefficients also has a relationship similar to equation (1) (Shi and Dozier, 1995; Shi et al., 1993; Singh and Venkataraman, 2009):

$$\sigma_t^{AP(vvhh)}(\theta_i) = \sigma_v^{AP(vvhh)}(\theta_r) + T_{AP(vvhh)}^2(\theta_i)\sigma_{sg}^{AP(vvhh)}(\theta_r), \tag{2}$$

where,

$$\sigma_t^{AP(vvhh)}(\theta_i) = \sqrt{VVHH} = \sqrt{\sigma_t^{vv}(\theta_i)\sigma_t^{hh}(\theta_i)}. \tag{3}$$

Where $\sigma_t^{AP(vvhh)}$, $\sigma_v^{AP(vvhh)}$, and $\sigma_{sg}^{AP(vvhh)}$ are the square root of the product of total, volume, and snow-ground interface VV and HH polarization backscattering coefficients, respectively. $T_{AP(vvhh)}$ is the square root of the product of Fresnel power transmissivity at the air-snow interface for polarization VV and HH.

An approach is developed for retrieving dry snow density with both volume backscattering and snow-ground interface backscattering. The

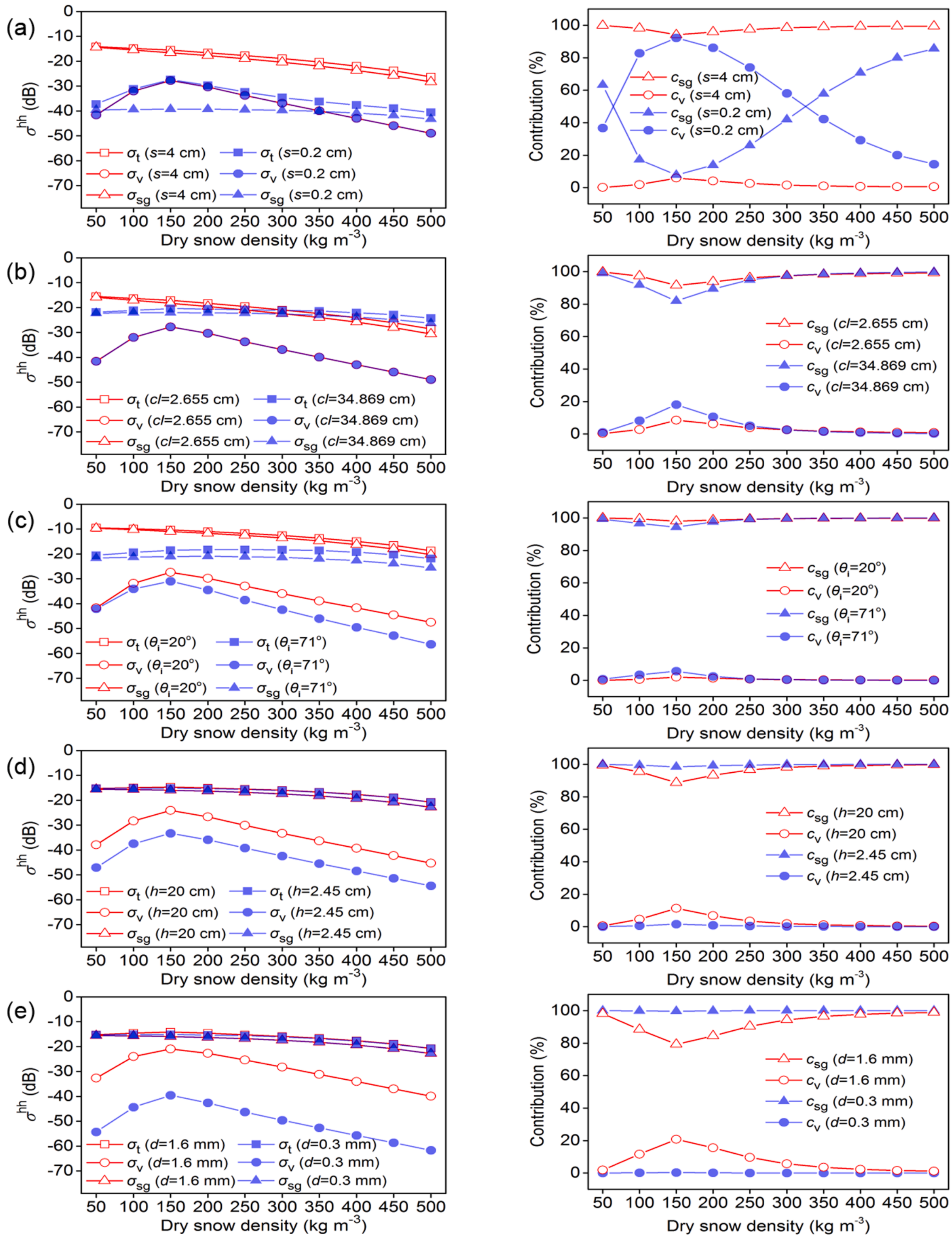

Fig. 4. Simulated relationships between dry snow density and the total, volume, and snow-ground interface backscattering coefficients in different simulation scenarios at the HH polarization of 5.405 GHz. The left panel of (a) - (e) is the results of two extreme RMS height, correlation length, incidence angle, snow depth, and snow grain diameter conditions, respectively. The right panel of (a) - (e) shows the corresponding snow-ground interface and volume backscattering contributions to total backscattering. The input of model was collected by the field experiments in MRA: incidence angle 43.45°, snow depth 8.66 cm, snow temperature 268.96 K, snow grain diameter 0.8 mm, QCA stickiness parameter 0.1, volumetric water content of snow and soil 0 and 2%, clay content weight fraction 0.217, soil RMS height 1.77 cm, and soil correlation length 13.275 cm. *s:* Soil RMS height, *cl:* Soil correlation length, *h:* Snow depth, *d:* Snow grain diameter, c_{sg}: Snow-ground interface backscattering contribution to total backscattering, c_v: Volume backscattering contribution to total backscattering.

volume backscattering is based on the Dense Media Radiative Transfer (DMRT) (Tsang et al., 1985; Wen et al., 1990) and the first-order volume scattering model is adopted. The single scattering AIEM is used in calculating the snow-ground interface backscattering. A new backscattering model at snow-ground interface is derived, which is simple and efficient for a wide range of roughness and incidence angles.

Snow-ground interface backscattering relationship: Firstly, the backscattering components of the snow-ground interface are simulated using

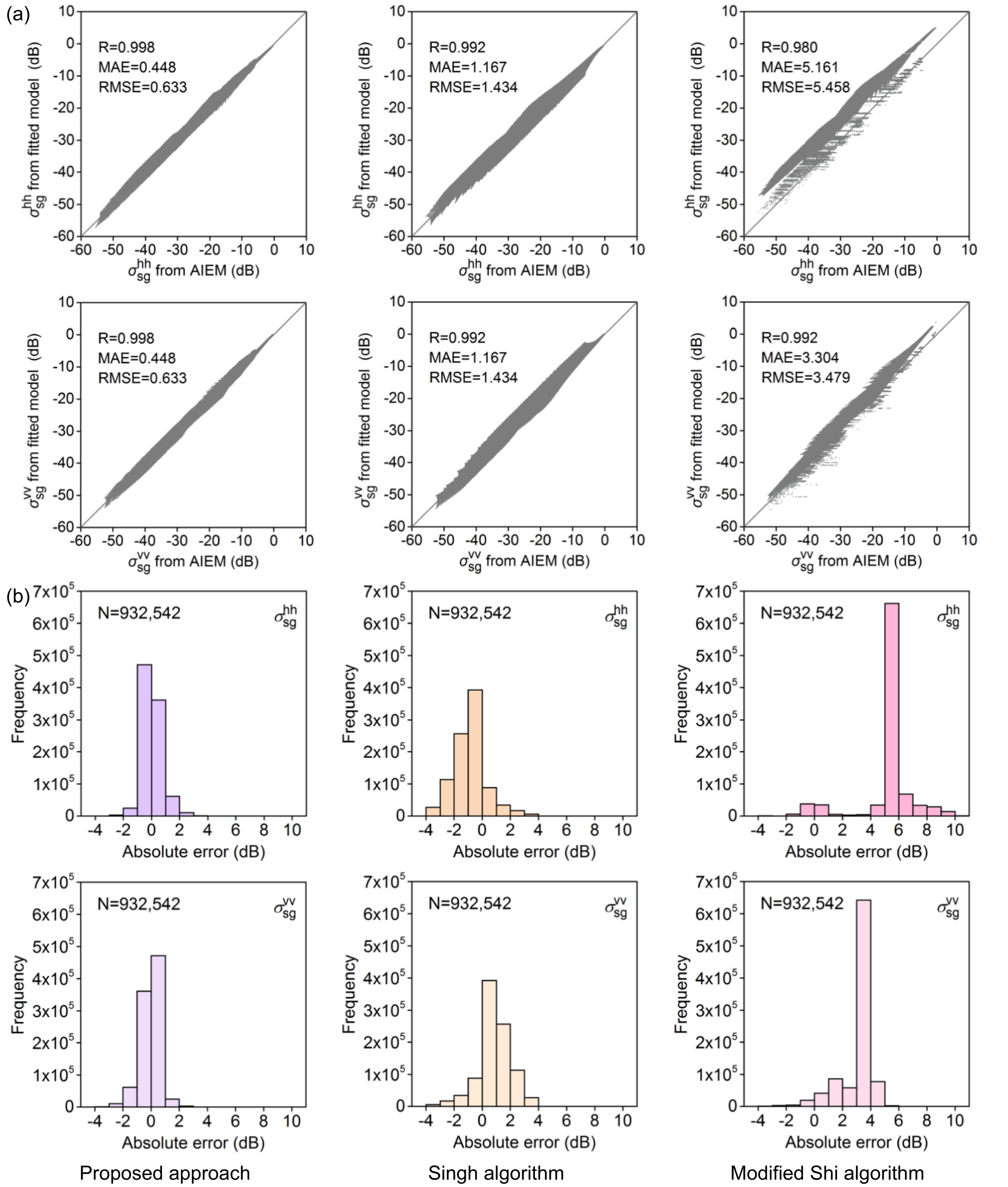

Fig. 5. Comparison of the AIEM and the fitted snow-ground interface models (a), and histogram of absolute errors for σ_{sg}^{hh} and σ_{sg}^{vv} between the AIEM model and the fitted model (b) used in the proposed approach, Singh algorithm, and modified Shi algorithm.

the AIEM model (Chen et al., 2000; 2003) in the range of snow densities of 90 kg m^{-3} to 320 kg m^{-3} under a wide range of dielectric, roughness, and incidence angles (Table 2). The most commonly used form of exponential surface correlation function to describe soil surface (Shi et al., 1997) is selected in the simulation. The range of each parameter is selected based on the measured data in MRA.

Secondly, based on the backscattering coefficients of common features at C-band, the simulation records with a backscattering coefficient (HH/VV/HV/VH) less than –100 dB or greater than 4 dB are removed.

Then, the relationship between HH and VV polarization backscat-

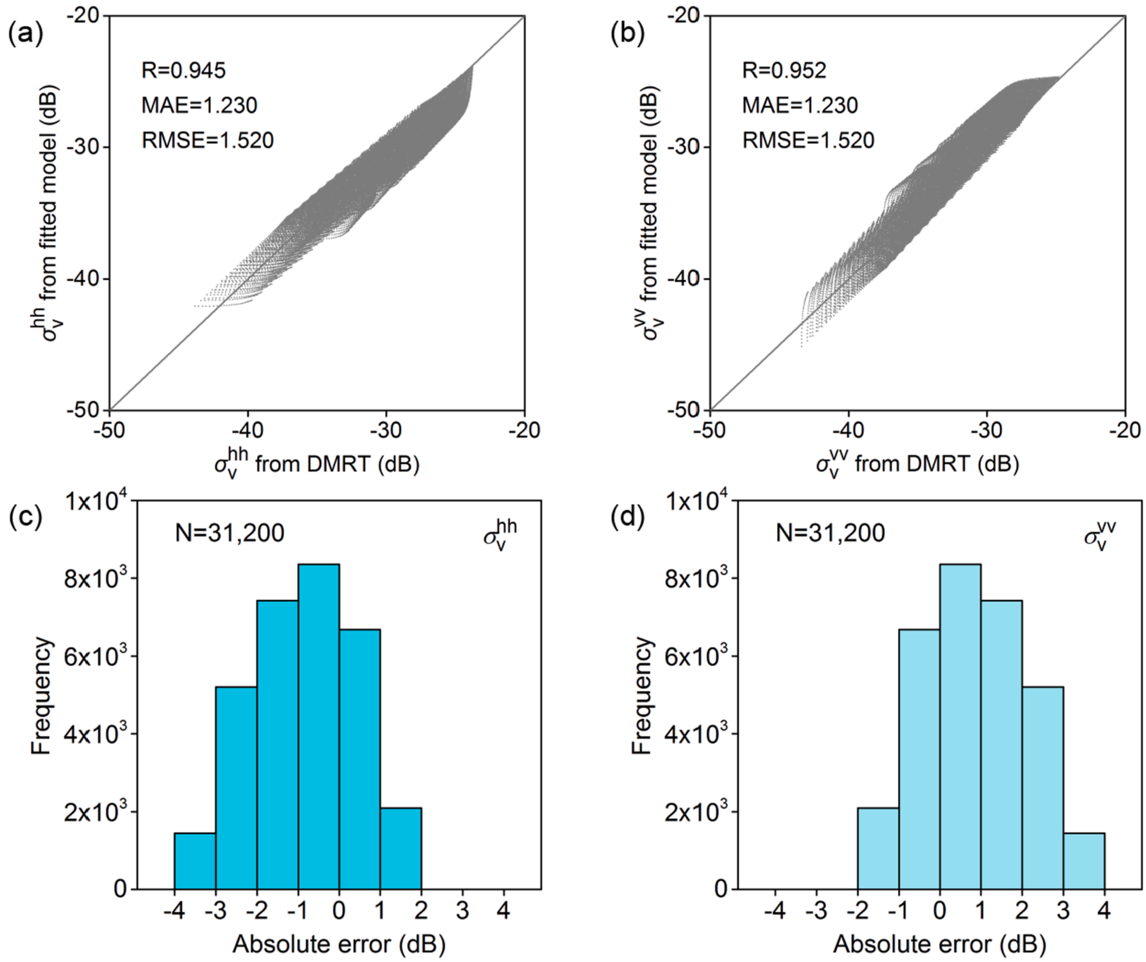

Fig. 6. Comparison of the fitted model and the DMRT model for σ_v^{hh} (a) and σ_v^{vv} (b), with the (c) and (d) being the corresponding histogram of absolute errors.

tering characteristics is described under the conditions of each incidence angle and wide range of surface roughness, and the coefficients of the fitted relationship are found by regression analysis.

$$\frac{\sqrt{\frac{\sigma_{sg}^{vv}}{\sigma_{sg}^{hh}}}}{\frac{|\alpha_{vv}(\theta_i,\varepsilon_s)|}{|\alpha_{hh}(\theta_i,\varepsilon_s)|}} \times \frac{|T_{vv}(\theta_i,\varepsilon_s)|}{|T_{hh}(\theta_i,\varepsilon_s)|} = 0.19 + 0.306 \times \frac{\sigma_{sg}^{vv}}{\sigma_{sg}^{hh}} - 0.088 \times \frac{|\alpha_{vv}(\theta_i,\varepsilon_s)|}{|\alpha_{hh}(\theta_i,\varepsilon_s)|}$$

$$+ 0.629 \times \frac{|T_{vv}(\theta_i,\varepsilon_s)|^2}{|T_{hh}(\theta_i,\varepsilon_s)|^2} \times \frac{|\alpha_{hh}(\theta_i,\varepsilon_s)|^2}{|\alpha_{vv}(\theta_i,\varepsilon_s)|^2} \ \left(R^2 = 0.991,\ p < 0.05\right), \tag{4}$$

where $\alpha_{pp}(\theta_i, \varepsilon_s)$ is the polarization amplitude for polarization pp in the small perturbation model.

Equation (4) represents the relationship between the backscattering coefficients of a large range random rough surfaces at a given incidence angle. This relationship minimizes sensitivity to the surface roughness and di-electricity, and maximizes sensitivity to the incidence angle.

Snow volume backscattering relationship (Shi and Dozier, 1995; Shi et al., 1993; Singh and Venkataraman, 2009): The first-order volume backscattering coefficients from a non-homogeneous dielectric half-space medium are functions of the incidence angle, surface roughness, permittivity, and volume scattering albedo:

$$\sigma_v^{pp} = \frac{3}{4}\omega T_{pp}^2 \times \text{loss factor}, \tag{5}$$

where loss factor explains the effect of rough surfaces on the transmission (Ulaby et al., 1982). ω is snow volume scattering albedo, depending on the liquid water content, particle size, density, size variation, and shape of snow (Tsang et al., 1992). It is independent of polarization supposing spherical or randomly oriented particles. Thus, the ratios of the first-order volume backscattering for different polarization are expressed as functions of snow relative permittivity and local incidence angle. $D_T(\theta_i, \varepsilon_s)$, $D_{TH}(\theta_i, \varepsilon_s)$, and $D_{TV}(\theta_i, \varepsilon_s)$ represent the volume backscattering ratios of VV to HH, $\sqrt{VVHH}$ to HH, and $\sqrt{VVHH}$ to VV, where ε_s is the relative permittivity of snowpack. These ratios constitute the volume backscattering relationships, which only rely on the local incidence angle and snow relative permittivity.

$$D_T(\theta_i, \varepsilon_s) = \frac{\sigma_v^{vv}}{\sigma_v^{hh}} = \frac{|T_{vv}(\theta_i,\varepsilon_s)|^2}{|T_{hh}(\theta_i,\varepsilon_s)|^2} \tag{6}$$

$$D_{TH}(\theta_i, \varepsilon_s) = \frac{\sigma_v^{AP(vvhh)}}{\sigma_v^{hh}} = \frac{|T_{AP(vvhh)}(\theta_i,\varepsilon_s)|^2}{|T_{hh}(\theta_i,\varepsilon_s)|^2} = \frac{|T_{vv}(\theta_i,\varepsilon_s)|}{|T_{hh}(\theta_i,\varepsilon_s)|} \tag{7}$$

$$D_{TV}(\theta_i, \varepsilon_s) = \frac{\sigma_v^{AP(vvhh)}}{\sigma_v^{vv}} = \frac{|T_{AP(vvhh)}(\theta_i,\varepsilon_s)|^2}{|T_{vv}(\theta_i,\varepsilon_s)|^2} = \frac{|T_{hh}(\theta_i,\varepsilon_s)|}{|T_{vv}(\theta_i,\varepsilon_s)|} \tag{8}$$

Inversion algorithm: Two relations can be derived based on best pairs. And the relations are only functions of the local incidence angle and snow relative permittivity.

$$\sigma_t^{AP(vvhh)} - D_{TV}(\theta_i,\varepsilon_s)\sigma_t^{vv} = T_{AP(vvhh)}^2\sigma_{sg}^{AP(vvhh)} - D_{TV}(\theta_i,\varepsilon_s)T_{vv}^2\sigma_{sg}^{vv} \tag{9}$$

$$\sigma_t^{vv} + \sigma_t^{hh} - \frac{D_{TV}(\theta_i,\varepsilon_s) + D_{TH}(\theta_i,\varepsilon_s)}{D_{TV}(\theta_i,\varepsilon_s)D_{TH}(\theta_i,\varepsilon_s)}\sigma_t^{AP(vvhh)}$$

$$= T_{vv}^2\sigma_{sg}^{vv} + T_{hh}^2\sigma_{sg}^{hh} - \frac{D_{TV}(\theta_i,\varepsilon_s) + D_{TH}(\theta_i,\varepsilon_s)}{D_{TV}(\theta_i,\varepsilon_s)D_{TH}(\theta_i,\varepsilon_s)}T_{AP(vvhh)}^2\sigma_{sg}^{AP(vvhh)} \tag{10}$$

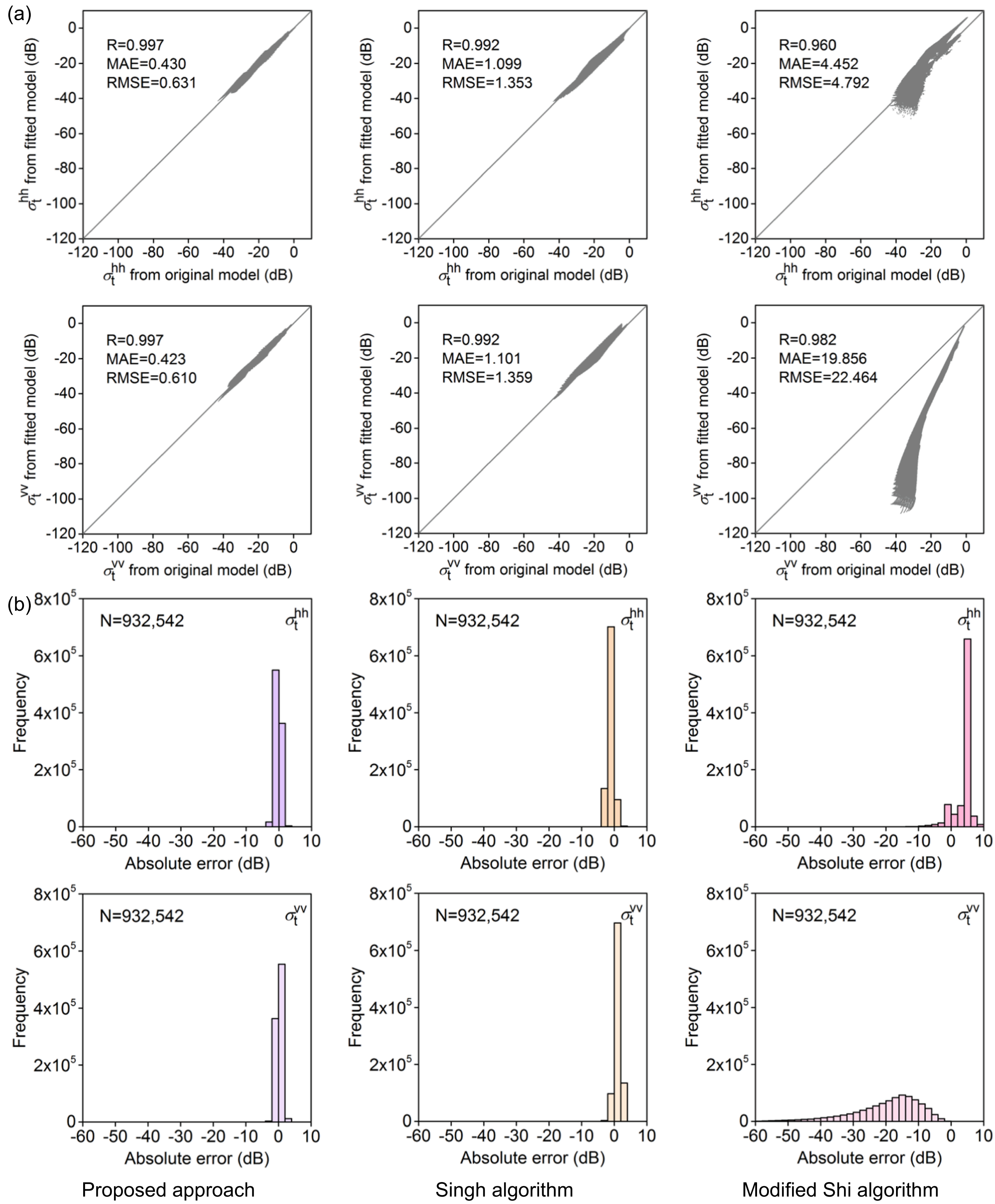

Fig. 7. Comparison of the original model and the fitted total models (a), and histogram of absolute errors for σ_t^{hh} and σ_t^{vv} between the original model and the fitted model (b) used in the proposed approach, Singh algorithm, and modified Shi algorithm.

Equations (4) to (10) can be used to derive the snow relative permittivity.

$$\sigma_t^{AP(vvhh)} = \frac{\sigma_t^{hh} \times \left(\frac{|T_{vv}(\theta_i,\varepsilon_s)|^2}{|T_{hh}(\theta_i,\varepsilon_s)|^2}\right) \times \sqrt{\frac{\sigma_{sg}^{vv}}{\sigma_{sg}^{hh}}} + \sigma_t^{vv}}{\left(\frac{|T_{vv}(\theta_i,\varepsilon_s)|}{|T_{hh}(\theta_i,\varepsilon_s)|}\right) \times \left(\sqrt{\frac{\sigma_{sg}^{vv}}{\sigma_{sg}^{hh}}} + 1\right)} \tag{11}$$

where (Singh and Venkataraman, 2009),

$$T_{hh}(\theta_i,\varepsilon_s) = \frac{2\sqrt{\varepsilon_s - \sin^2\theta_i}}{\cos\theta_i + \sqrt{\varepsilon_s - \sin^2\theta_i}} \tag{12}$$

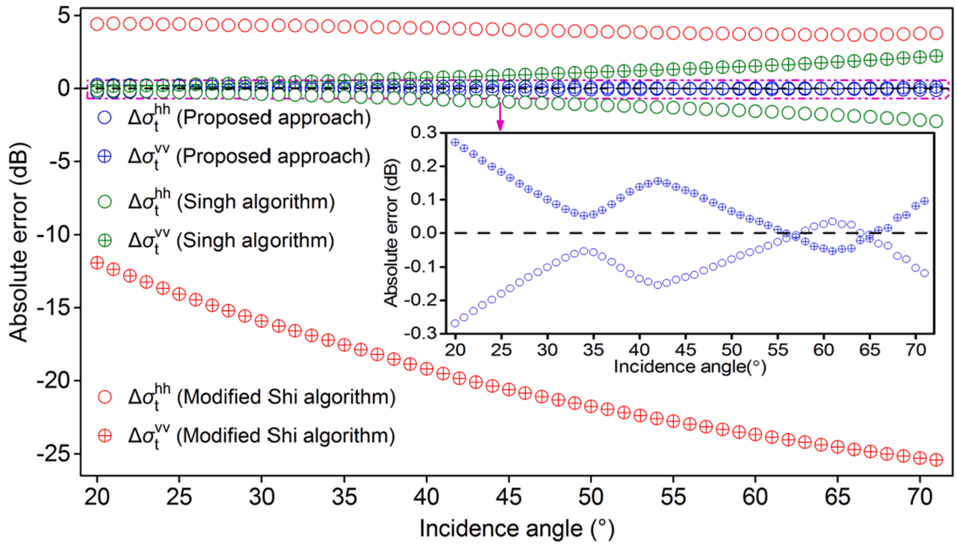

Fig. 8. Absolute errors between the fitted model and the original model varying with incidence angles.

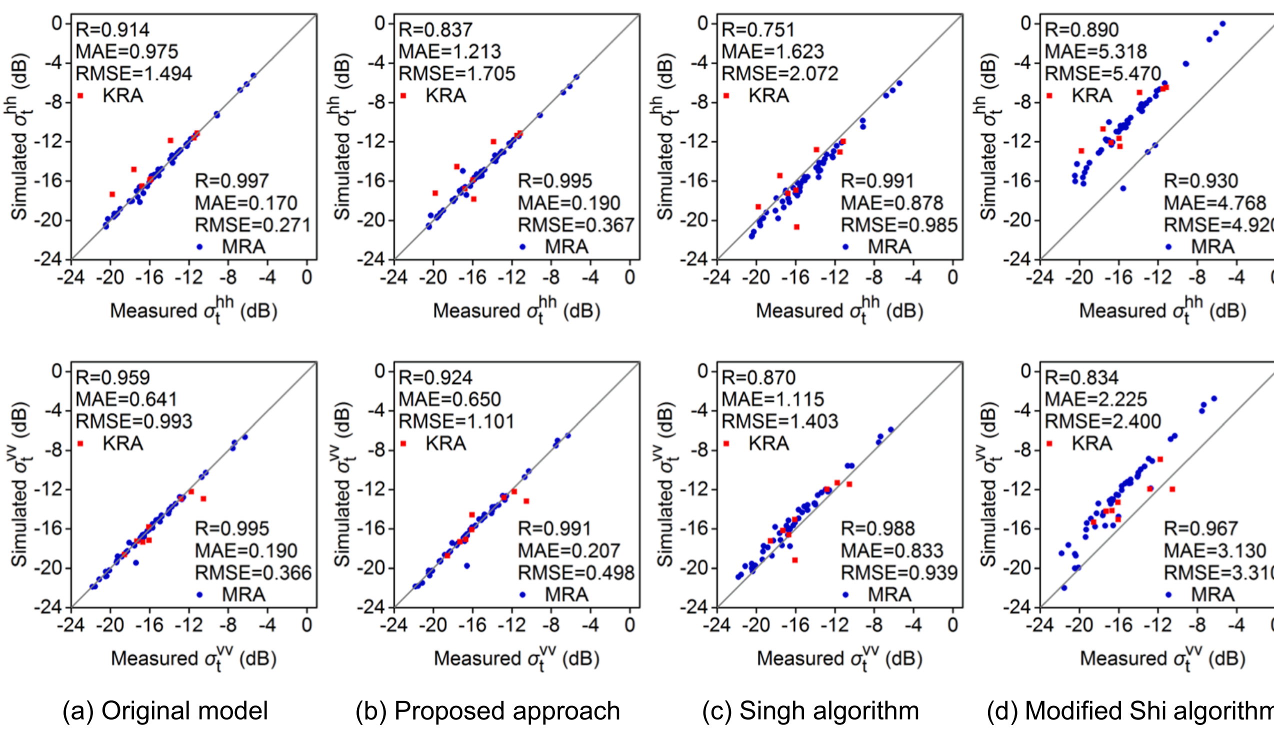

Fig. 9. Evaluation of the original model (a), proposed approach (b), Singh algorithm (c), and modified Shi algorithm (d), with the top and bottom panel being the results of HH and VV, respectively.

$$T_{vv}(\theta_i,\varepsilon_s)=\frac{2\sqrt{\varepsilon_s-\sin^2\theta_i}}{\varepsilon_s\cos\theta_i+\sqrt{\varepsilon_s-\sin^2\theta_i}} \tag{13}$$

$$\alpha_{hh}(\theta_i,\varepsilon_s)=\frac{\cos\theta_i-\sqrt{\varepsilon_s-\sin^2\theta_i}}{\cos\theta_i+\sqrt{\varepsilon_s-\sin^2\theta_i}} \tag{14}$$

$$\alpha_{vv}(\theta_i,\varepsilon_s)=(\varepsilon_s-1)\frac{\sin^2\theta_i-\varepsilon_s\left(1+\sin^2\theta_i\right)}{\left(\varepsilon_s\cos\theta_i+\sqrt{\varepsilon_s-\sin^2\theta_i}\right)^2} \tag{15}$$

where $\sqrt{\frac{\sigma_{sg}^{vv}}{\sigma_{sg}^{hh}}}$ is approximately calculated from equation (4).

Moreover, Looyenga's semi-empirical dielectric formula (Looyenga, 1965) can be used to estimate dry snow density in good agreement with Polder and van Santen's physical formula (Matzler, 1996).

$$\varepsilon_s=1.0+1.5995\rho_s+1.861\rho_s^3\left(\rho_s\le 0.5\ \mathrm{g\,cm^{-3}}\right), \tag{16}$$

where ρ_s is the snow density.

3.2. Methods for comparison

Singh algorithm: An algorithm was developed for dry snow density estimation by Singh and Venkataraman (2009) considering both volume backscattering and snow-ground interface backscattering. The volume backscattering relationships were the same as equation (6) to (8) using the first-order volume backscattering model. And the snow-ground

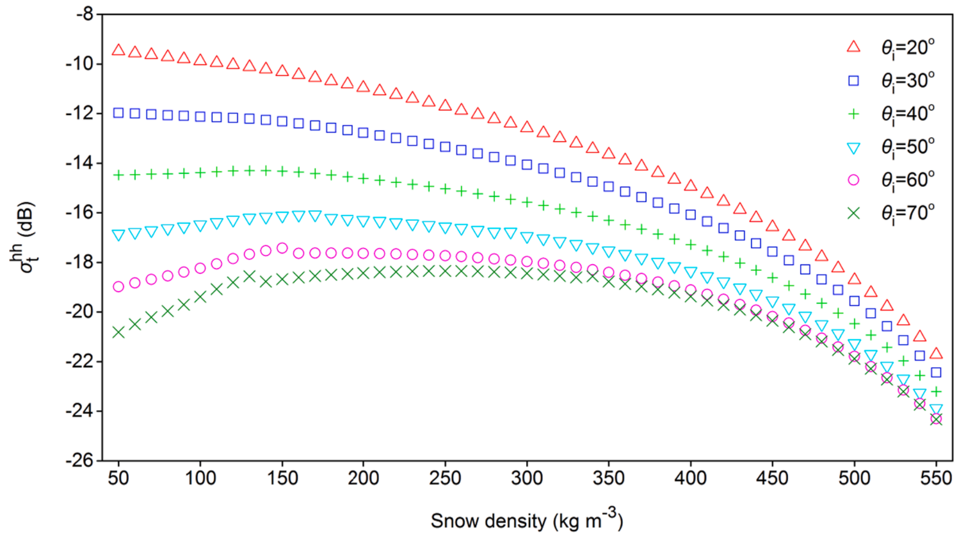

Fig. 10. Sensitivity of the proposed approach for HH polarization backscattering to incidence angle and snow density.

interface relationship (Shi et al., 1993) was found using best pair of polarization based on the SPM model (Valenzuela, 1967).

Modified Shi algorithm: An algorithm was developed for dry snow density estimation by Shi and Dozier (2000) only considering snow-ground interface backscattering. The L-band data were simulated using the IEM model and the snow-ground interface relationship was found using regression analysis.

In order to retrieve snow density using the Shi algorithm based on C-band data, the Shi algorithm suitable for L-band is modified for C-band.

The backscattering coefficients simulated by the AIEM model (Chen et al., 2000; 2003) in the proposed approach are regressed to redefine the coefficients of Shi snow-ground interface relationship. The modified snow-ground interface relationship is

$$\log_{10}\left[\sqrt{\sigma_{sg}^{hh}}+\sqrt{\sigma_{sg}^{vv}}\right]=0.151+0.5\times\log_{10}\left(\sigma_{sg}^{hh}+\sigma_{sg}^{vv}\right)+0.001\times\log_{10}\left(\frac{\sigma_{sg}^{hh}}{\sigma_{sg}^{vv}}\right)-0.066\times\log_{10}\left(\frac{\sigma_{sg}^{hh}}{\sigma_{sg}^{vv}}\right)^2\quad(\mathrm{R}^2=1,\ \mathrm{p}<0.05),\tag{17}$$

where $\log_{10}\left(\sigma_{sg}^{hh}\right)$ is automatically excluded because of collinearity.

The modified algorithm is

$$\log_{10}\left[\frac{\sqrt{\sigma_t^{hh}}}{T_{hh}(\theta_i,\varepsilon_s)}+\frac{\sqrt{\sigma_t^{vv}}}{T_{vv}(\theta_i,\varepsilon_s)}\right]=0.151+0.5\times\log_{10}\left[\frac{\sigma_t^{hh}}{T_{hh}^2(\theta_i,\varepsilon_s)}+\frac{\sigma_t^{vv}}{T_{vv}^2(\theta_i,\varepsilon_s)}\right]+0.001\times\log_{10}\left[\frac{\sigma_t^{hh}T_{vv}^2(\theta_i,\varepsilon_s)}{\sigma_t^{vv}T_{hh}^2(\theta_i,\varepsilon_s)}\right]-0.066\times\log_{10}\left[\frac{\sigma_t^{hh}T_{vv}^2(\theta_i,\varepsilon_s)}{\sigma_t^{vv}T_{hh}^2(\theta_i,\varepsilon_s)}\right]^2.\tag{18}$$

4. Results

4.1. Effects of snow density on C-band backscattering

The backscattering of dry snow is sensitive to the snow density and other snow features. The dry snow density dependence of backscattering is shown in Fig. 4, where the input parameters calculated by the model are based on field and SAR measurements in MRA. The measured mean and extreme values of snow depth, snow temperature, snow grain diameter, soil RMS height, and soil correlation length are adopted. Although the centre incidence angle of SAR is fixed, the local incidence angle varies greatly due to the influence of mountainous terrain. The centre and extreme incidence angles measured by SAR are used.

The results show that the snow-ground interface backscattering is dominant for C-band generally being much larger than the snow volume backscattering. However, for low-density dry snow with a density between 100 kg m^{-3} and 250 kg m^{-3}, snow volume backscattering cannot be ignored. Specially, snow volume backscattering is dominant when the soil RMS height is small. The difference in soil RMS height, snow grain diameter, soil correlation length, snow depth, and incidence angle all affects surface and volume backscattering contributions to total backscattering. The degree of influence decreases in turn. Moreover, the volume backscattering increases first and then decreases with the increasing of snow density, and reaches the maximum at the snow density of 150 kg m^{-3}. In addition, the snow-ground interface backscattering decreases with the increasing of snow density when the snow density is greater than 250 kg m^{-3}. It is greatly affected by the surface roughness, which should be weakened when the snow parameters are retrieved.

At a constant density, the volume scattering albedo increases with the increasing of snow grain diameter. The volume backscattering increases with the increasing of snow depth. Moreover, in general, soil RMS height and incidence angle are two major factors affecting the total backscattering. The maximum difference in total backscattering is approximately 23 dB at the soil RMS heights of 0.2 cm and 4 cm. It is about 11 dB at the incidence angles of 20° and 71°.

Therefore, the relationship between backscattering and dry snow density is controlled by the scattering mechanism and depends on incidence angle, surface roughness, and snow cover characteristics. The factors make it possible to improve the snow density inversion algorithm for C-band data.

4.2. Fitting of backscattering model

It is generally believed that the closer the results of the fitted relationship are to the simulation results of the original model, the higher the accuracy of the inversion results using the fitted model.

Fitting of snow-ground interface backscattering model: The HH and VV polarization backscattering at snow-ground interface from the fitted model are compared with the original simulation data from the AIEM

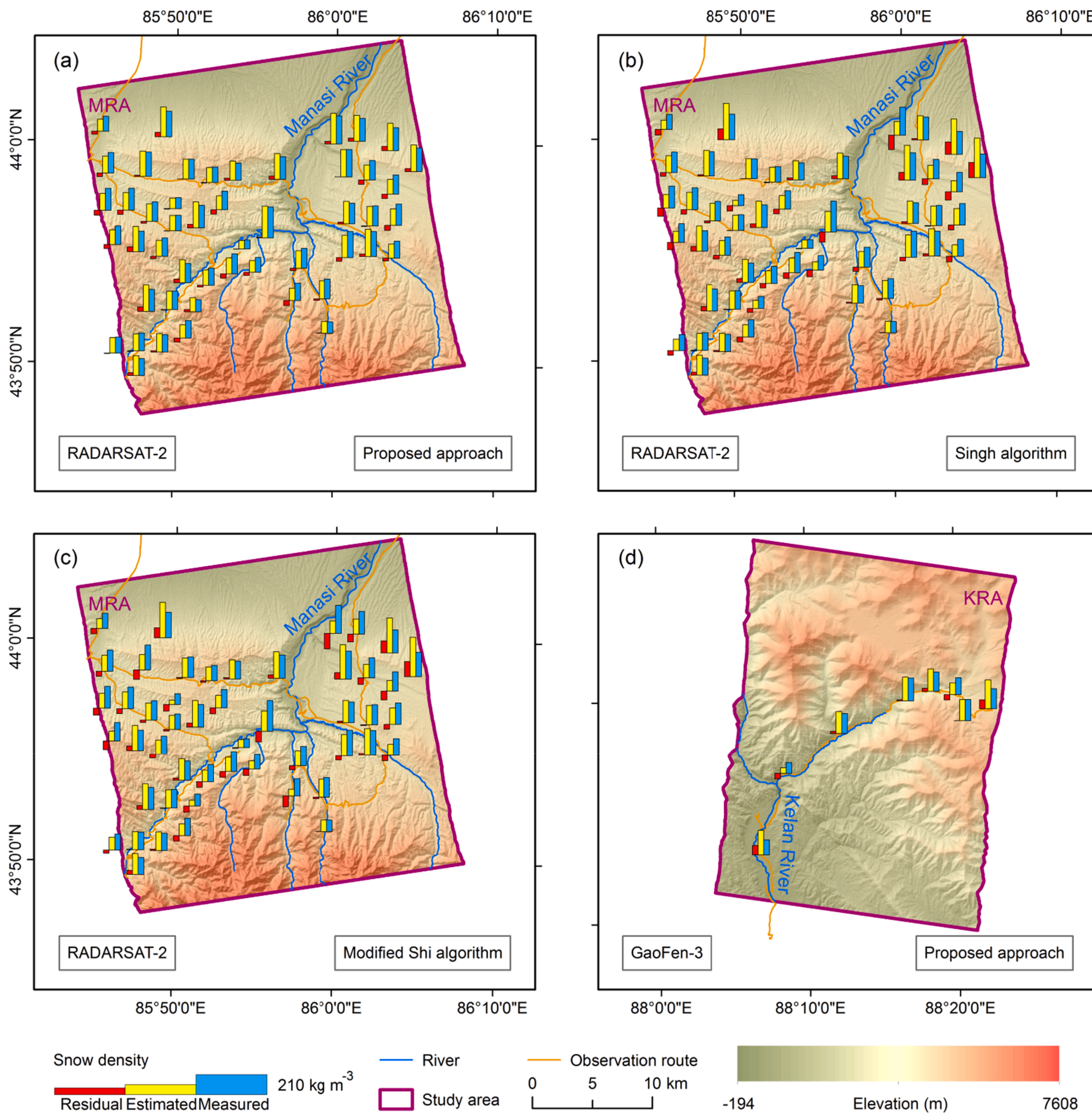

Fig. 11. Residual distribution of the snow density in MRA retrieved using the proposed approach (a), Singh algorithm (b), modified Shi algorithm (c), and in KRA using the proposed approach (d).

model (Chen et al., 2000; 2003), and histograms of absolute errors are shown based on the proposed approach, Singh algorithm, and modified Shi algorithm (Fig. 5). The results based on the proposed approach are better than the Singh algorithm and the modified Shi algorithm. The correlation coefficient (R), mean absolute error (MAE), and root mean square error (RMSE) of the proposed approach are 0.998, 0.448 dB, and 0.633 dB, respectively. 89% of the absolute errors are concentrated between plus and minus 1 dB. The R, MAE, and RMSE based on the Singh algorithm are 0.992, 1.167 dB, and 1.434 dB, respectively. Different from them, the Rs, MAEs, and RMSEs based on the modified Shi algorithm have substantial difference between HH (0.980, 5.161 dB, and 5.458 dB) and VV (0.992, 3.304 dB, and 3.479 dB). It may be caused by the removal of the $\log_{10}\left(\sigma_{sg}^{hh}\right)$ in equation (17) during regression. Many horizontal lines on the comparison figures reveal simple parameter settings of the fitted model. In the modified Shi algorithm, better results are mostly observed when the value of incidence angle, surface roughness, or soil moisture is close to the boundary values.

Fitting of snow volume backscattering model: The HH and VV polarization volume backscattering from the fitted model are compared with the original simulation data from the DMRT model (Tsang et al., 1985; Wen et al., 1990), and histograms of absolute errors are shown (Fig. 6). Parameters used to simulate are listed in Table 3. 79% of the absolute errors are concentrated between plus and minus 2 dB. Many horizontal and vertical lines on the comparison figures show that the parameter settings of the fitted model can be improved.

Fitting of dry snow total backscattering model: Based on the proposed approach, Singh algorithm, and modified Shi algorithm, the total HH and VV polarization backscattering from the fitted model are compared with the original simulation data from the AIEM and DMRT model, and histograms of absolute errors are shown (Fig. 7). 91% and 54% of the absolute errors are concentrated between plus and minus 1 dB using the

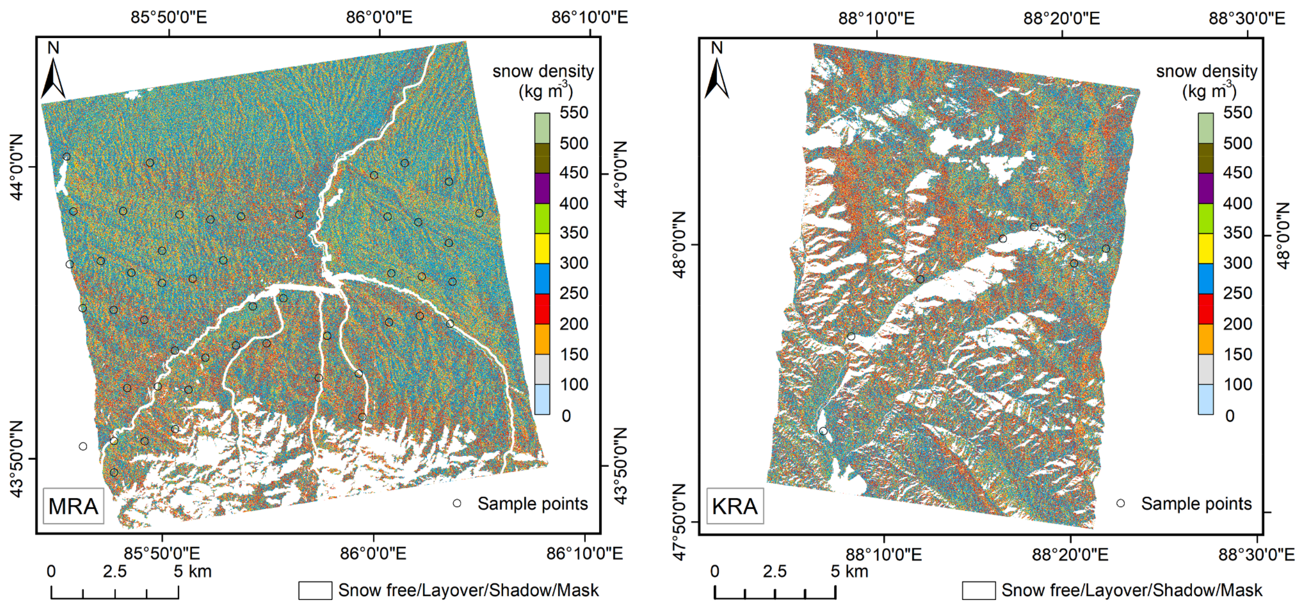

Fig. 12. Dry snow density maps retrieved using the proposed approach in MRA and KRA.

proposed approach and Singh algorithm, respectively. The modified Shi algorithm does not perform as well as the other two methods. It may be due to the fact that the modified Shi algorithm only considers the backscattering at the snow-ground interface, especially the VV polarization backscattering is greatly affected. In the modified Shi algorithm, the points with better results mostly meet the conditions of small incidence angle or surface roughness or soil moisture.

As can be seen from Fig. 8, the absolute error between the fitted model and the original model using the proposed approach varies between plus and minus 0.271 dB as the incidence angles increase. When the incidence angle is greater than 23°, the absolute error varies between plus and minus 0.2 dB. When the incidence angle is 57° or 65°, it is close to 0. It means that when the incidence angle is about 57° or 65°, the fitted model can replace the original model. The absolute error by the Singh algorithm increases with the increasing of incidence angles. When the incidence angle is less than 34°, the absolute error is between plus and minus 0.5 dB. The absolute error for σ_t^{hh} by the modified Shi algorithm decreases slightly as the incidence angles increase. On the contrary, the absolute error for σ_t^{vv} increases significantly.

4.3. Comparison of the model and SAR measurements

In order to evaluate the applicability of the original backscattering model and three methods for snow density inversion in the two study areas, the simulated backscattering coefficients are compared with the C-band SAR measurements (Fig. 9). The snow and soil parameters measured at each sampling point are used in the simulation.

Model simulations are consistent with SAR measurements. Consistency is higher in MRA than in KRA. This is mainly because the snow is dry in MRA and not completely dry in KRA. The consistency of the original model, proposed approach, Singh algorithm, and modified Shi algorithm decreases in turn.

In MRA, the σ_t^{hh} and σ_t^{vv} of the proposed approach are very consistent with the RADARSAT-2 measurements. The RMSEs from all 49 sampling points are 0.367 dB and 0.498 dB for HH and VV polarizations. While in KRA, they are generally consistent with the GaoFen-3 measurements. The corresponding RMSEs from all 8 sampling points are 1.705 dB and 1.101 dB.

4.4. Sensitivity of the proposed approach

The proposed approach is only sensitive to the incidence angle and density. In the simulation, the fixed input parameters are the same as those in Fig. 4, and the variable input parameters include the incidence angle and snow density. We set the incidence angle in the range of 20°–70°, the step size is 10°, the snow density is in the range of 50–550 kg m^{-3}, and the step size is 10 kg m^{-3}.

The results are shown in Fig. 10. Under the same incidence angle, the HH polarization backscattering at an incidence angle up to 30° decreases gradually, and the HH polarization backscattering at an incidence angle greater than or equal to 40° increases first and then decreases with the increasing of snow density, with slight fluctuations in the middle. The difference between the maximum and minimum values is approximately 12 dB. It can be seen that the cut-off point is at a density of 150 kg m^{-3}, and the slight fluctuations are also nearby. This phenomenon is caused by the different properties of dry snow. The snow with a density up to 150 kg m^{-3} is dominated by fresh snow and has not been densified. The greater the density, the more ice crystal particles, and the stronger the volume backscattering signal of dry snow. While the density is greater than 150 kg m^{-3}, the snow has been densified. The stronger the coherent scattering between dense media, the weaker the volume backscattering signal of dry snow. This further confirms the conclusion that snow volume backscattering cannot be ignored for low-density dry snow with a density between 100 kg m^{-3} and 250 kg m^{-3} in Subsection 4.1. It is also the inadequacy of some algorithms. Under the same density, the HH polarization backscattering decreases steadily as the incidence angle increases, and the difference between the maximum and minimum values is about 11 dB.

4.5. Inversion of dry snow density

In KRA, the inversion values at some measured points using the Singh algorithm and modified Shi algorithm are beyond the theoretical range of dry snow density. The residual distribution of the snow density retrieved using the three methods in MRA and proposed approach in KRA are shown in Fig. 11. In MRA, the points with large residuals using the modified Shi algorithm are distributed mainly in the northwest, northeast, and south. Large residuals using the Singh algorithm appear mainly in the northeast. Using the proposed approach, the residuals are all small. In KRA, the points with large residuals using the proposed

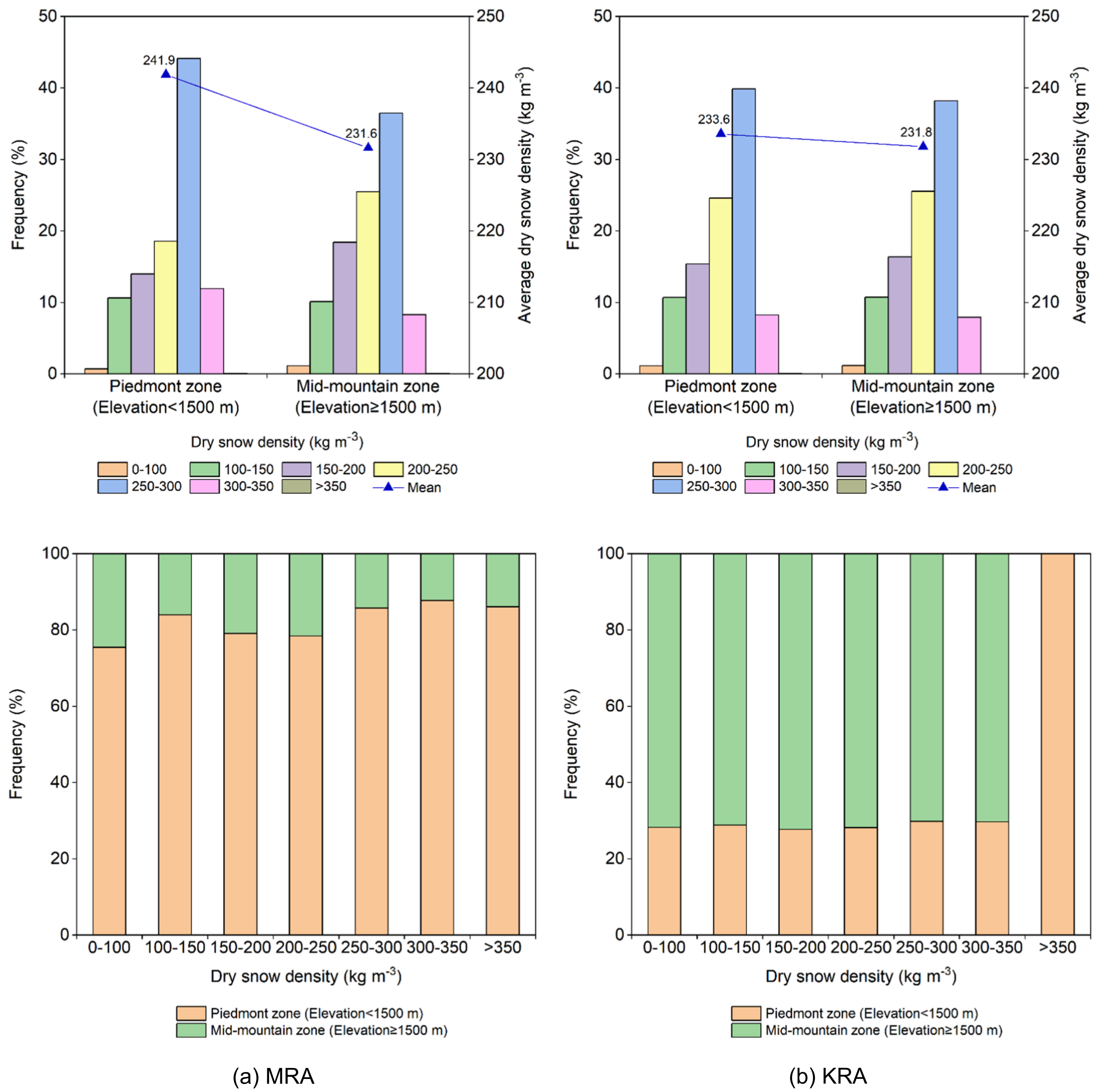

Fig. 13. Distribution of dry snow density at different elevations (top), and elevation with different dry snow densities (bottom) in MRA (a) and KRA (b).

approach are distributed mainly in the east and south.

Dry snow density maps in the two study areas retrieved using the proposed approach are shown in Fig. 12. The average dry snow density in MRA and KRA is 239.2 kg m^{-3} and 234.6 kg m^{-3}, respectively. The range of dry snow density is concentrated in 90 kg m^{-3} to 320 kg m^{-3}, consistent with field measurements (simulation range). Only 7.6% of the snow-covered pixels are outside the simulation range in MRA, and 8.2% in KRA. These small ratios confirm the good performance of the proposed approach and small impact by different incidence angles.

The out-of-range values mainly come from two aspects: areas with very small incidence angles and areas with a HH/VV ratio of greater than 1. As mentioned above (Fig. 8), the performance of the proposed approach degrades when the incidence angle is up to 23°. In MRA, the average HH and VV polarization backscattering coefficients outside the range are 0.050 (–13.042 dB) and 0.041 (–13.875 dB) respectively, and the average HH/VV ratio is 1.220 (0.862 dB). In KRA, the corresponding values are 0.297 (–5.273 dB), 0.246 (–6.096 dB), and 1.209 (0.823 dB), respectively. This is because the snow beyond the range is disturbed by human activities. According to the physical analysis (Yueh et al., 2009), there are two decisive factors for the HH/VV ratio greater than 1. One is the volume scattering of vegetation with horizontal arrangement phenology on snow, and the other is the double bounce scattering effect between the snow-ground interface and vegetation particularly in the shallow snow areas. The influence of these two factors is not considered in any of the three methods in this study. Because more sunlight can be received on the southern slope, the out-of-range values on the southern slope are about three times that on the northern slope in MRA, and it is about twice in KRA. Forest, water bodies, and artificial surfaces are masked. The average of window with 5 × 5 pixels is used to fill in the values outside our simulation range.

The study areas are at moderate to lower elevation, and the dry snow density decreases slightly with the increase of elevation (Fig. 13). This may be because the lower elevation area is affected by human activities. Trampling on snow caused by frequent human and livestock activities

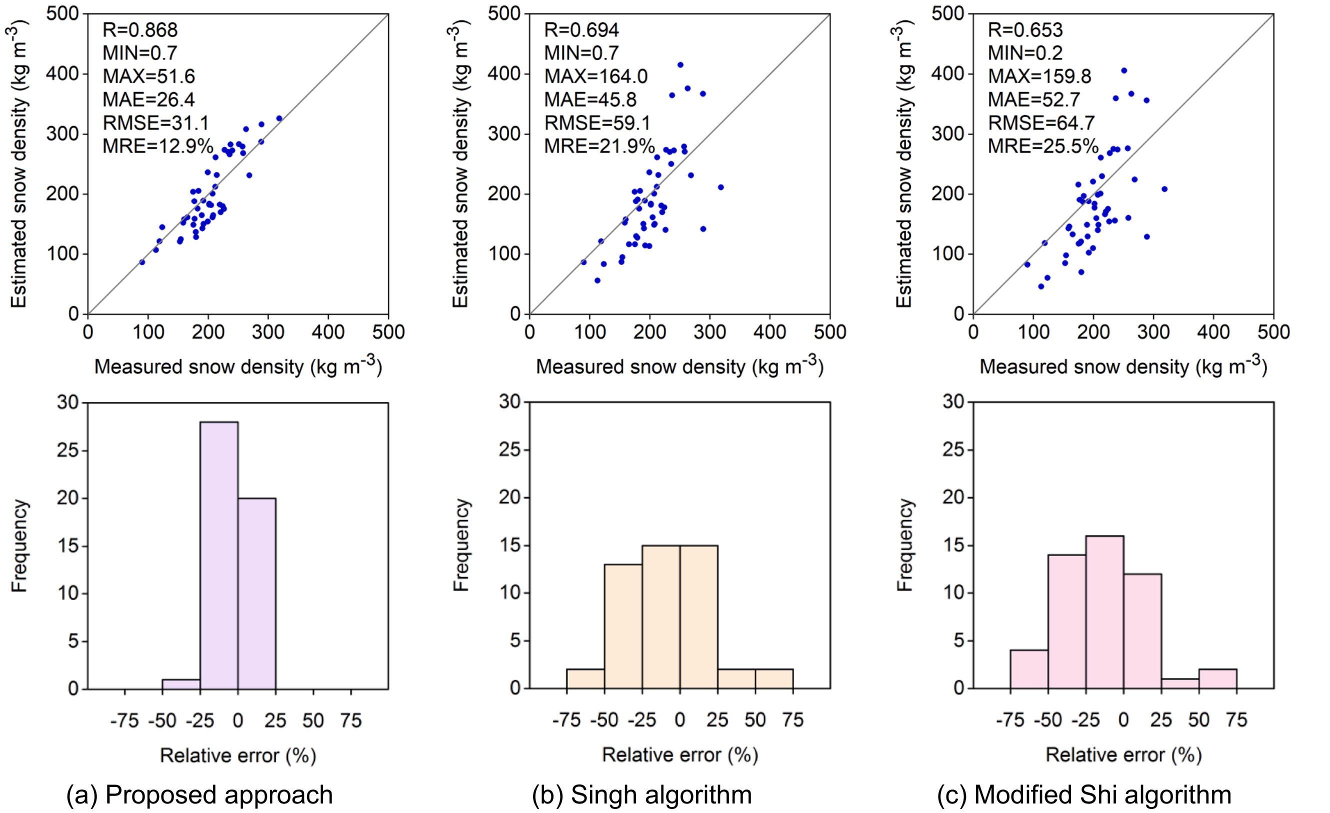

Fig. 14. Comparison of field measurements with the snow density estimated from C-band RADARSAT-2 data (top), and histogram of relative errors (bottom). The three panels represent method takes proposed approach (a), Singh algorithm (b), and modified Shi algorithm (c). MIN: Minimum absolute error, MAX: Maximum absolute error, MRE: Mean relative error.

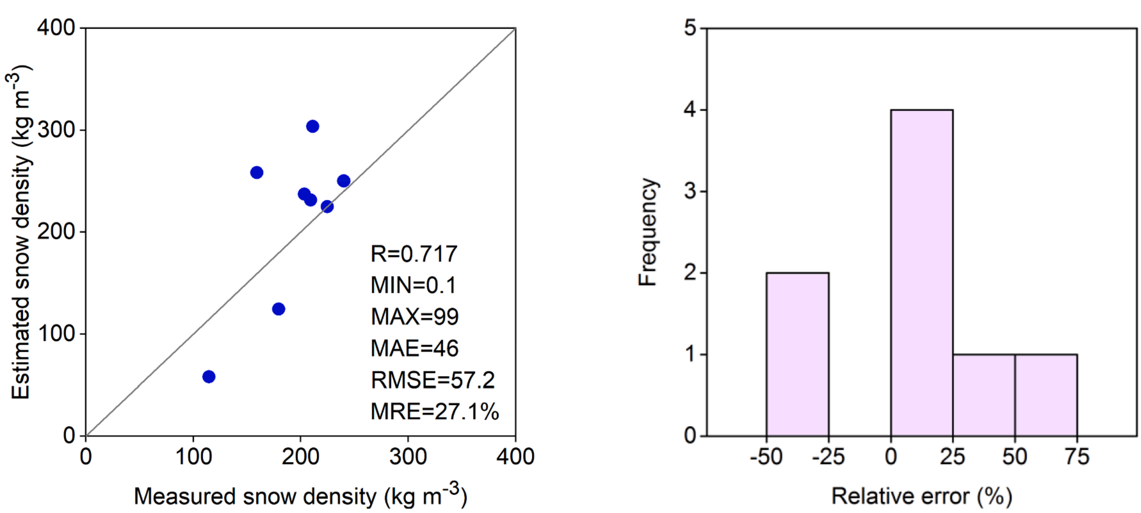

Fig. 15. Comparison of field measurements with the snow densities estimated from C-band GaoFen-3 data (a), and histogram of relative errors (b).

results in a slight increase in dry snow density. Dry snow density is mainly 250–300 kg m^{-3}, with little presence greater than 350 kg m^{-3}. The distribution of dry snow with various densities in the two study areas is completely opposite. In MRA, more than 75% are distributed at lower elevation, while in KRA, the proportion is less than 30%. The spatial distribution of retrieved snow density is in good agreement with regional conditions.

4.6. Accuracy of dry snow retrieval

According to the in-situ measurements collected in the field, the inversion results of dry snow density from different data in the two areas are statistically compared. The retrieved density is compared with the average value of snow layer.

In MRA, the comparisons are made with the data at 49 high confidence points collected during the field survey. The RMSE, mean relative error (MRE), and R of the snow density with the proposed approach are 31.1 kg m^{-3}, 12.9%, and 0.868, respectively, and the relative errors of snow density are concentrated between plus and minus 25%. The scatter plots and relative error frequency histograms of dry snow density measurements and density values retrieved by different methods are shown in Fig. 14. It can be seen that the proposed approach is superior to

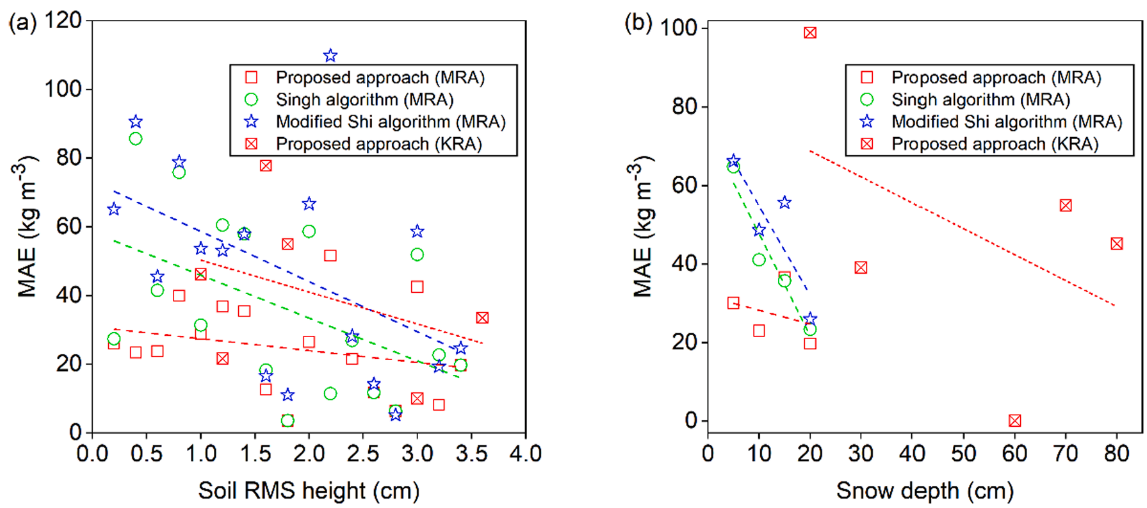

Fig. 16. Error response of modeling density corresponding to soil RMS height (a) and snow depth (b) for the proposed approach, Singh algorithm, and modified Shi algorithm in MRA and KRA.

the Singh algorithm and the modified Shi algorithm. As we mentioned earlier, for low-density snow with snow density ranging from 100 kg m^{-3} to 250 kg m^{-3}, the influence of volume scattering on snow density inversion at C-band cannot be ignored. Moreover, the AIEM model (Chen et al., 2000; 2003) with a more accurate description of random rough surface scattering is better than the SPM model (Valenzuela, 1967) suitable for small terrain fluctuations. Therefore, both the proposed approach and the Singh algorithm considering the volume scattering are superior to the modified Shi algorithm without considering the volume scattering, while the proposed approach based on the AIEM model (Chen et al., 2000; 2003) is better than the Singh algorithm based on the SPM model (Valenzuela, 1967). In addition, it has been verified in Subsection 4.2.

In KRA, the comparisons are made with the data at 8 high confidence points collected during the field survey. Fig. 15 compares field measurements of snow density with estimates from GaoFen-3 data using the proposed approach. The RMSE, MRE, and R of the snow density are 57.2 kg m^{-3}, 27.1%, and 0.717, respectively, and half the relative errors of snow density are concentrated in 0–25%. Despite some deviations, the estimated snow densities are in good agreement with the field measurements. Snow depth up to 78 cm has little effect on the inversion approach.

The volumetric water content of snow at the top two points with the large deviation in the figure is 0.76% at 15 cm to 25 cm and 0.68% at 5 cm to 15 cm, respectively. When the snow surface is very dry, the radar can detect deeper places, while when the snow surface is wet, the wet layer contributes more to the radar signal, and the radar may not be able to detect the layer below it. The proposed approach is dominated by the backscattering from the underlying surface of snow. The simple average method used may not truly represent the snow density detected by radar. From this verification, it can be concluded that the proposed approach is suitable for the maximum volumetric water content of snow at 0 to 25 cm not exceeding 0.68%, and the volumetric water content of the bottom snow not exceeding 7.89%.

5. Discussion

5.1. Advantages of the proposed approach

In most snow density inversion methods, e.g., the Shi algorithm, scattering mechanism was considered incomplete. The Singh algorithm fully considered the scattering mechanism, but it was only suitable for a narrow range of incidence angles, limited to 31.0°–36.3° and slightly rough surfaces. The proposed approach improves the Singh algorithm with C-band HH and VV measurements based on a large number of simulated backscattering coefficients by fully considering the scattering mechanism. It is suitable for incidence angles of 20°–71° and soil roughness with an RMS height up to 4 cm, and correlation length up to 35 cm. The approach minimizes the sensitivity to surface dielectric and roughness properties while maximizing the sensitivity to incidence angle. It does not need a prior knowledge of the underlying dielectric and roughness properties.

5.2. Influence of topography

In mountainous areas with complex terrain, terrain will have a significant impact on radar backscattering (Goyal et al., 1999; Ladson and Moore, 1992). Teillet et al. (1985) found that the uncertainty of radar backscattering caused by terrain factors is 8%–38% in Canadian mountains. The influence of terrain on radar backscattering is mainly caused by affecting the local incidence angle and the interaction mechanism between radar and ground objects. While the proposed approach minimizes the influence of topography, resulting in acceptable inversion accuracy, it is necessary to calculate the local incidence angle by DEM with higher accuracy and spatial resolutions for higher inversion accuracy.

5.3. Error response

The proposed approach is obtained based on the range of the measured data in MRA, and then verified in KRA. Although reliable inversions have been obtained in both study areas, the error response is evident in the comparison of the two study areas.

Error response with respect to measurement methods: Some studies have shown that while snow fork measurements are reliable, snow density is underestimated compared to other physical measurement methods (Lemmetyinen et al., 2016; Techel and Pielmeier, 2011a; Tiuri et al., 1984). Moldestad (2005) reported negligible errors of snow density determined by snow forks as low as plus and minus 5 kg m^{-3}. The inversion results in MRA are relatively balanced, and most snow densities in KRA are overestimated. It may be related to whether snow densities are all measured by snow forks in the two study areas.

Error response with respect to model parameters: The potential errors of the proposed approach mainly come from the assumptions of soil RMS height, snow depth, and volumetric water content of snow.

The soil RMS height in MRA ranges from 0.2 cm to 3.4 cm, and it is set to 0.2 cm to 4 cm in the proposed approach accordingly. The snow depth in the proposed approach is based on the average snow depth of

Table A1
Measured snow and soil parameters.

Study area	Sample	Snow parameters							Soil parameters	
		Density (kg m^{-3})	Depth (cm)	Grain diameter (mm)	Temperature (K)	Stratification	Volumetric water content (%)	Layer	RMS height (cm)	Correlation length (cm)
MRA	1	180	12.5	0.8	269.1	3	0	–	2.2	2.5
	2	220.7	10.5	0.63	269.6	2	0	–	0.8	32.5
	3	226	9.45	0.83	269.1	2	0	–	1.2	12.5
	4	212	15.95	0.8	270.85	3	0	–	1.2	12.5
	5	190.1	11	1.15	271.15	3	0	–	0.6	12.5
	6	227.3	5.5	0.8	268.96	1	0	–	0.4	12.5
	7	207.2	6	0.45	270.15	2	0	–	0.8	22.5
	8	237.3	5	0.45	270.15	1	0	–	1.4	22.5
	9	262.9	4.65	0.7	268.35	1	0	–	0.6	22.5
	10	199.1	10.5	0.63	269.6	2	0	–	0.8	32.5
	11	224.2	6.3	1	269.95	2	0	–	1.4	32.5
	12	208.3	14.4	0.8	268.96	3	0	–	1.2	22.5
	13	179.5	5.85	0.8	270.25	1	0.23	1st	3	32.5
	14	192.1	10	0.9	270.35	2	0	–	0.4	22.5
	15	199.4	8.5	0.8	270	2	0	–	1.4	32.5
	16	233.2	15.75	0.67	270	3	0	–	1	12.5
	17	268.4	4	1	271.3	1	0	–	0.8	22.5
	18	219.1	4.9	0.7	268.35	1	0	–	1	32.5
	19	240.2	4	0.55	268.96	1	0	–	1.4	2.5
	20	152.9	8.5	0.7	268.96	2	0	–	1	12.5
	21	235.5	6	0.6	268.96	2	0	–	0.2	2.5
	22	174.7	5.5	1.42	266.55	1	0	–	1.6	12.5
	23	154.2	2.45	0.7	268.96	1	0	–	0.8	12.5
	24	288.8	4.5	0.6	268.96	1	0	–	0.4	12.5
	25	175.2	10	1	271.3	2	0	–	2	12.5
	26	189.4	16.5	0.8	268.96	4	0	–	2.4	32.5
	27	204.6	11	0.8	268.96	3	0	–	0.6	12.5
	28	256.9	5.5	1	271.3	1	0	–	2.4	22.5
	29	184	7.95	0.93	270.1	2	0.35	bottom	2.4	22.5
	30	123.7	8.45	0.8	263.9	2	0	–	0.2	22.5
	31	201.8	7	0.9	270.35	2	0	–	3.4	12.5
	32	177.3	10.2	0.8	270	2	0	–	0.4	12.5
	33	214.3	5.8	1	271.3	1	0	–	1.4	32.5
	34	201.6	15.5	0.8	268.96	3	0	–	2.4	32.5
	35	176.6	8	1.42	266.55	2	0	–	2.6	12.5
	36	257.8	6.95	0.75	269.25	2	0	–	1	32.5
	37	318.2	5.5	0.8	268.96	1	0	–	3.2	22.5
	38	182.3	6.2	1.42	266.55	2	0	–	2.8	12.5
	39	113	10	0.9	270.35	2	0	–	0.4	12.5
	40	207.2	9	0.63	269.6	2	0	–	1.6	32.5
	41	158.2	10	1.15	271.15	2	0	–	1.8	22.5
	42	251.1	6.45	0.45	270.15	2	0	–	0.8	2.5
	43	165.2	6.5	1.42	266.55	2	0	–	1.2	2.5
	44	90	6.95	0.8	272.75	2	0	–	0.6	12.5
	45	191.8	7.95	0.99	262.45	2	0	–	1.8	32.5
	46	118.8	20	0.8	268.96	4	0	–	1.6	12.5
	47	160.1	18	0.67	270	4	0	–	1.8	2.5
	48	288.1	5.1	0.45	270.15	1	0	–	0.4	2.5
	49	211.9	8	0.9	269.85	2	0	–	0.6	22.5
KRA	1	211.5	78.3	0.8	265.16	8	0.76	3rd	1	22.5
							0.6	5th		
							0.11	6th		
							0.23	7th		
							7.83	bottom		
	2	225.1	58.1	0.8	264.07	6	0.22	3rd	1	12.5
	3	179.5	62.73	1	263.99	6	0.34	2nd	1.8	12.5
	4	203.7	78	0.8	264.71	8	0.12	bottom	3.6	12.5
	5	240.1	71.37	0.95	264.39	7	7.89	bottom	3	32.5
	6	209.5	30.13	0.8	267.25	3	0.11	bottom	1.2	12.5
	7	114.5	25.97	0.9	266.02	2	0.54	bottom	1.6	22.5
	8	159.2	20.37	1.2	267.02	2	0.32	1st	1.6	22.5
							0.68	bottom		

8.66 cm in MRA. The MAE in snow density for each method shows a linear downtrend relative to the soil RMS height (snow depth), and the proposed approach is the gentlest one (Fig. 16). It can be considered that this method is relatively robust to small changes in soil RMS height (snow depth), that is, it is low sensitive to soil RMS height (snow depth). This has also been verified in KRA, although the verification results are general. Therefore, the proposed approach is suitable for the soil RMS height of 0.2–4 cm, and the snow depth of 0–78 cm.

The reason for the unsatisfactory results in KRA is that the snow is not completely dry. This is most obvious at a two-layer observation point. The volumetric water content of the first layer and the bottom layer is 0.32% and 0.68%, respectively. An explanation is given in Subsection 4.6.

5.4. Limitations of the proposed approach

Since the proposed approach is mainly based on the correction of surface scattering problem, it can be applied to the seasonal snow cover with dry snow with a subsurface of either soil or rock. However, it cannot be applied to the vegetated area where volume scattering is dominant.

The proposed approach was obtained using the range of the measurements from MRA and was applied to KRA. The MRA is a mountainous area while the KRA has a relatively flat surface. Despite the difference of the two focus areas in view of snow properties and topography, the proposed approach showed a relatively stable accuracy for both areas, suggesting a satisfactory generalization capability. However, more validation should be made for operational uses.

The inversion results of snow density in the study areas show that the proposed approach can be applied to a large range of incidence angles (20°–71°). The sensitivity analysis shows that the proposed approach depends on the incidence angle. The optimal incidence angle for the proposed approach is about 57° or 65° because the absolute error is closest to 0 compared with the original model. However, the coefficients of the fitted model are fixed values. It maybe leads to the limited inversion accuracy when the proposed approach is applied in other areas, despite the good inversion results in the study areas. The coefficients of the fitted model are best expressed functions of the incidence angle and wavenumber. Firstly, the fitted model in functional form is more accurate than that in fixed form. Secondly, the inversion accuracy will not be greatly affected when different C-band data are used in other areas. A more accurate expression of coefficients is the next step to be studied.

The classical Shi fitted model is used for the fitting of volume scattering, and the response law of volume scattering to density is very obvious. How to further efficiently modify the volume scattering fitted model and improve the inversion accuracy remain to be discussed in the next step.

6. Conclusion

In this study, an improved approach to retrieve snow density using C-band co-polarization SAR data is proposed based on a wide range of parameter simulation, with two main modifications compared to existing methods. The proposed approach fully considered the scattering mechanism with wider valid incidence angles of 20°–71° and a wider roughness range (RMS height $\leq$ 4 cm, correlation length $\leq$ 35 cm). And the Shi algorithm suitable for L-band is modified to be suitable for C-band. In addition, we selected the RADARSAT-2 data obtained in MRA on December 13, 2013 and GaoFen-3 data obtained in KRA on January 17, 2018 to retrieve the snow density. The two types of SAR data differed in satellite orbits, sensors, location, acquisition time, and snow conditions. These differences can serve as evaluation criteria for the applicability of the proposed approach under various conditions. The inverted snow density agrees well with the field measurements. The small RMSEs and relative errors demonstrate the reliability of the proposed approach. The inversion accuracy of the proposed approach is higher than that of the Singh algorithm and modified Shi algorithm. At the same time, it is found that the snow depth up to 78 cm has little effect on the inversion approach. The inversion approach is suitable for the case that the maximum volumetric water content of 0–25 cm snow does not exceed 0.68%, and that of the bottom snow does not exceed 7.89%.

However, vegetation has a great impact on the proposed approach. Whether it is applicable to other uses is still unresolved. In addition, the coefficients of fitted model expressed as functions of the incidence angle and wavenumber, and correction of volume scattering fitted model may improve the inversion accuracy.

Declaration of Competing Interest

The authors declare that they have no known competing financial interests or personal relationships that could have appeared to influence the work reported in this paper.

Acknowledgments

This work was supported by the National Natural Science Foundation of China under Grant No. 42171307 and the Science & Technology Basic Resources Investigation Program of China under Grant No. 2017FY100502. The authors would like to thank the China Centre for Resources Satellite Data and Application for the kindly providing the GaoFen-3 data. They would also like to thank the field observers who obtained the valuable near-synchronous field measurements from the two study areas.

Appendix A

References

Abe, T., Yamaguchi, Y., Sengoku, M., 1990. Experimental study of microwave transmission in snowpack. IEEE Trans. Geosci. Remote Sens. 28 (5), 915–921.
Awasthi, S., Thakur, P.K., Kumar, S., Kumar, A., Jain, K., Mani, S., 2020. Snow density retrieval using hybrid polarimetric RISAT-1 datasets. IEEE J. Sel. Top. Appl. Earth Observ. Remote Sens. 13, 3058–3065.
Bernier, M., Fortin, J.P., 1998. The potential of times series of C-band SAR data to monitor dry and shallow snow cover. IEEE Trans. Geosci. Remote Sens. 36 (1), 226–243.
Brucker, L., Royer, A., Picard, G., Langlois, A., Fily, M., 2011. Hourly simulations of the microwave brightness temperature of seasonal snow in Quebec, Canada, using a coupled snow evolution–emission model. Remote Sens. Environ. 115 (8), 1966–1977.
Brun, E., David, P., Sudul, M., Brunot, G., 1992. A numerical model to simulate snow-cover stratigraphy for operational avalanche forecasting. J. Glaciol. 38, 13–22.
Chen, K.S., Wu, T.D., Tsay, M.K., Fung, A.K., 2000. A note on the multiple scattering in an IEM model. IEEE Trans. Geosci. Remote Sens. 38, 249–256.
Chen, K.S., Wu, T.D., Tsang, L., Li, Q., Shi, J., Fung, A.K., 2003. Emission of rough surfaces calculated by the integral equation method with comparison to three-dimensional moment method simulations. IEEE Trans. Geosci. Remote Sens. 41, 90–101.
Conde, V., Nico, G., Mateus, P., Catalão, J., Kontu, A., Gritsevich, M., 2019. On the estimation of temporal changes of snow water equivalent by spaceborne SAR interferometry: a new application for the Sentinel-1 mission. J. Hydrol. Hydromech. 67 (1), 93–100.
Dai, L., Che, T., Wang, J., Zhang, P., 2012. Snow depth and snow water equivalent estimation from AMSR-E data based on a *priori* snow characteristics in Xinjiang, China. Remote Sens. Environ. 127, 14–29.
DeBeer, C.M., Pomeroy, J.W., 2010. Simulation of the snowmelt runoff contributing area in a small alpine basin. Hydrol. Earth Syst. Sci. 14, 1205–1219.
Elder, K., Dozier, J., Michaelsen, J., 1991. Snow accumulation and distribution in an Alpine Watershed. Water Resour. Res. 27 (7), 1541–1552.
Engman, E.T., Chauhan, N., 1995. Status of microwave soil moisture measurements with remote sensing. Remote Sens. Environ. 51 (1), 189–198.
Frost, V.S., Stiles, J.A., Shanmugan, K.S., Holtzman, J.C., 1982. A model for radar images and its application to adaptive digital filtering of multiplicative noise. IEEE Trans. Pattern Anal. Mach. Intell. PAMI-4 (2), 157–166.
Fung, A.K., 1994. Microwave scattering and emission models and their applications. Artech House, Norwood, MA.
Fung, A.K., Li, Z., Chen, K.S., 1992. Backscattering from a randomly rough dielectric surface. IEEE Trans. Geosci. Remote Sens. 30 (2), 356–369.
Gray, D.M., 1970. Snow measurement in the prairie. Can. Agric. Eng. 12, 38–41.
Goyal, S.K., Seyfried, M.S., O'Neill, P.E., 1999. Correction of surface roughness and topographic effects on airborne SAR in mountainous rangeland areas. Remote Sens. Environ. 67 (2), 124–136.
Guneriussen, T., Hogda, K.A., Johnsen, H., Lauknes, I., 2001. InSAR for estimation of changes in snow water equivalent of dry snow. IEEE Trans. Geosci. Remote Sens. 39 (10), 2101–2108.
He, G., Xiao, P., Feng, X., Zhang, X., Wang, Z., Chen, N., 2015. Extracting snow cover in mountain areas based on SAR and optical Data. IEEE Geosci. Remote Sens. Lett. 12, 1136–1140.
Hirashima, H., Abe, O., Sato, A., Lehning, M., 2009. An adjustment for kinetic growth metamorphism to improve shear strength parameterization in the snowpack model. Cold Reg. Sci. Tech. 59 (2-3), 169–177.
Jonas, T., Marty, C., Magnusson, J., 2009. Estimating the snow water equivalent from snow depth measurements in the Swiss Alps. J. Hydrol. 378 (1-2), 161–167.

Ladson, A.R., Moore, I.D., 1992. Soil water prediction of the Konza Prairie by microwave remote sensing and topographic attributes. J. Hydrol. 138, 385–407.
Lemmetyinen, J., Schwank, M., Rautiainen, K., Kontu, A., Parkkinen, T., Mätzler, C., Wiesmann, A., Wegmüller, U., Derksen, C., Toose, P., Roy, A., Pulliainen, J., 2016. Snow density and ground permittivity retrieved from L-band radiometry: Application to experimental data. Remote Sens. Environ. 180, 377–391.
Li, H., Wang, Z., He, G., Man, W., 2017. Estimating snow depth and snow water equivalence using repeat-pass interferometric SAR in the northern piedmont region of the tianshan mountains. J. Sens. 2017, 1–17.
Li, Z., Guo, H., Shi, J., 2001. Retrieving dry snow density with SIR-C polarimetric SAR data. Sci. Bull. 46, 1211–1214.
Looyenga, H., 1965. Dielectric constants of heterogeneous mixtures. Physica. 31 (3), 401–406.
Ma, W., Xiao, P., Zhang, X., Song, Y., Ma, T., Ye, L., 2020. Retrieving snow wetness based on surface and volume scattering simulation. ISPRS-J. Photogramm. Remote Sens. 169, 17–28.
Martinec, J., Rango, A., 1986. Parameter values for snowmelt runoff modelling. J. Hydrol. 84 (3-4), 197–219.
Matzler, C., 1996. Microwave permittivity of dry snow. IEEE Trans. Geosci. Remote Sens. 34 (2), 573–581.
Meløysund, V., Leira, B., Høiseth, K.V., Lisø, K.R., 2007. Predicting snow density using meteorological data. Meteorol. Appl. 14 (4), 413–423.
Moldestad, D.A., 2005. Characterisation of liquid water content and snow density in a cross-country race ski track. Bull. Glaciol. Res. 22, 39–49.
Santi, E., Brogioni, M., Leduc-Leballeur, M., Macelloni, G., Montomoli, F., Pampaloni, P., Lemmetyinen, J., Cohen, J., Rott, H., Nagler, T., 2021. Exploiting the ANN potential in estimating snow depth and snow water equivalent from the airborne SnowSAR data at X-and Ku-Bands. IEEE Trans. Geosci. Remote Sens. 60, 1–16.
Shi, J., Dozier, J., 1995. Inferring snow wetness using C-band data from SIR-C's polarimetric synthetic aperture radar. IEEE Trans. Geosci. Remote Sens. 33, 905–914.
Shi, J., Dozier, J., 2000. Estimation of snow water equivalence using SIR-C/X-SAR, Part I: Inferring snow density and subsurface properties. IEEE Trans. Geosci. Remote Sens. 38, 2465–2474.
Shi, J., Dozier, J., Davis, R.E., 1990. Simulation of snow-depth estimation from multi-frequency radar. In, 10th Annual International Symposium on Geoscience and Remote Sensing (pp. 1129-1132): IEEE.
Shi, J., Dozier, J., Rott, H., 1993. Deriving snow liquid water content using C-band polarimetric SAR. IEEE, pp. 1038–1041.
Shi, J., Du, Y., Du, J., Jiang, L., Chai, L., Mao, K., Xu, P., Ni, W., Xiong, C., Liu, Q., Liu, C., Guo, P., Cui, Q., Li, Y., Chen, J., Wang, A., Luo, H., Wang, Y., 2012. Progresses on microwave remote sensing of land surface parameters. Sci. China- Earth Sci. 55, 1052–1078.
Shi, J., Wang, J., Hsu, A.Y., O'Neill, P.E., Engman, E.T., 1997. Estimation of bare surface soil moisture and surface roughness parameter using L-band SAR image data. IEEE Trans. Geosci. Remote Sens. 35, 1254–1266.
Sihvola, A., Tiuri, M., 1986. Snow fork for field determination of the density and wetness profiles of a snow pack. IEEE Trans. Geosci. Remote Sens. GE-24 (5), 717–721.
Singh, G., Venkataraman, G., 2009. Snow density estimation using polarimitric ASAR data. II-, 630-II-633.
Singh, G., Verma, A., Kumar, S., Snehmani, Ganju, A., Yamaguchi, Y., Kulkarni, A.V., 2017. Snowpack density retrieval using fully polarimetric TerraSAR-X data in the Himalayas. IEEE Trans. Geosci. Remote Sens. 55 (11), 6320–6329.
Singh, G., Yamaguchi, Y., Park, S.E., 2013. General four-component scattering power decomposition with unitary transformation of coherency matrix. IEEE Trans. Geosci. Remote Sens. 51 (5), 3014–3022.
Sturm, M., Taras, B., Liston, G.E., Derksen, C., Jonas, T., Lea, J., 2010. Estimating snow water equivalent using snow depth data and climate classes. J. Hydrometeorol. 11, 1380–1394.
Surendar, M., Bhattacharya, A., Singh, G., Venkataraman, G., 2015. Estimation of snow density using full-polarimetric synthetic aperture radar (SAR) data. Phys. Chem. Earth. 83-84, 156–165.
Techel, F., Pielmeier, C., 2011a. Point observations of liquid water content in wet snow–investigating methodical, spatial and temporal aspects. Cryosphere. 5 (2), 405–418.
Techel, F., Pielmeier, C., Schneebeli, M., 2011b. Microstructural resistance of snow following first wetting. Cold Reg. Sci. Technol. 65 (3), 382–391.
Teillet, P.M., Guindon, B., Meunier, J.F., Goodenough, D.G., 1985. Slope-aspect effects in synthetic aperture radar imagery. Can. J. Remote Sens. 11 (1), 39–49.
Tiuri, M., Sihvola, A., Nyfors, E., Hallikaiken, M., 1984. The complex dielectric constant of snow at microwave frequencies. IEEE J. Ocean. Eng. 9 (5), 377–382.
Tsang, L., Kong, J.A., Shin, R.T., 1985. Theory of microwave remote sensing. Reading, Wiley Interscience.
Tsang, L., Ding, K., Wen, B., 1992. Dense media radiative transfer theory for dense discrete random media with particles of multiple sizes and permittivities. Prog. Electromagn. Res. 6, 181–225.
Ulaby, F.T., Moore, R.K., Fung, A.K., 1982. Microwave remote sensing: Active and passive. Volume 2-Radar remote sensing and surface scattering and emission theory. Reading, MA: Addison-Wesley.
Valenzuela, G., 1967. Depolarization of EM waves by slightly rough surfaces. IEEE Trans. Antennas Propag. 15 (4), 552–557.
Varade, D., Manickam, S., Dikshit, O., Singh, G., Snehmani, 2020a. Modelling of early winter snow density using fully polarimetric C-band SAR data in the Indian Himalayas. Remote Sens. Environ., 240, 111699.
Varade, D., Maurya, A.K., Dikshit, O., Singh, G., Manickam, S., 2020b. Snow depth in Dhundi: an estimate based on weighted bias corrected differential phase observations of dual polarimetric bi-temporal Sentinel-1 data. Int. J. Remote Sens. 41 (8), 3031–3053.
Snehmani, Venkataraman, G., Nigam, A.K., Singh, G., 2010. Development of an inversion algorithm for dry snow density estimation and its application with ENVISAT-ASAR dual co-polarization data. Geocarto Int. 25 (8), 597–616.
Wen, B., Tsang, L., Winebrenner, D.P., Ishimaru, A., 1990. Dense medium radiative transfer theory: Comparison with experiment and application to microwave remote sensing and polarimetry. IEEE Trans. Geosci. Remote Sens. 28 (1), 46–59.
Yueh, S.H., Dinardo, S.J., Akgiray, A., West, R., Cline, D.W., Elder, K., 2009. Airborne Ku-band polarimetric radar remote sensing of terrestrial snow cover. IEEE Trans. Geosci. Remote Sens. 47 (10), 3347–3364.
Zhong, X., Zhang, T., Wang, K., 2014. Snow density climatology across the former USSR. Cryosphere. 8 (2), 785–799.
Zhuo, Y., Xiao, P., Feng, X., Zhang, X., Yang, Y., Ye, L., Li, C., Hu, R., Bian, G., 2017. Spatial distribution and features of the snow cover during accumulation period in the middle reaches of the Kelan River, Altay region, Xinjiang. J. Glaciol. Geocryol. 39, 979–988.